Constraining the population of 6 ? z ? 10 star-forming galaxies with deep near-IR images of lensing clusters

J. Richard, R. Pelló, D. Schaerer, J.-F. Le Borgne, J.-P. Kneib

To cite this version:

J. Richard, R. Pelló, D. Schaerer, J.-F. Le Borgne, J.-P. Kneib. Constraining the population of 6 ? z ? 10 star-forming galaxies with deep near-IR images of lensing clusters. 2023. hal-00193525

HAL Id: hal-00193525

https://hal.science/hal-00193525v1

Preprint submitted on 5 Sep 2023

Astronomy & Astrophysics manuscript no. highz˙photo˙v5.8
August 30, 2021

Constraining the population of $6 \lesssim z \lesssim 10$ star-forming galaxies with deep near-IR images of lensing clusters *

J. Richard[1,5], R. Pelló[1], D. Schaerer[2,1], J.-F. Le Borgne[1], and J.-P. Kneib[3,4]

[1] Observatoire Midi-Pyrénées, Laboratoire d'Astrophysique, UMR 5572, 14 Avenue E. Belin, F-31400 Toulouse, France
[2] Geneva Observatory, 51 Ch. des Maillettes, CH–1290 Sauverny, Switzerland
[3] OAMP, Laboratoire d'Astrophysique de Marseille, UMR 6110 traverse du Siphon, 13012 Marseille, France
[4] Caltech Astronomy, MC105-24, Pasadena, CA 91125, USA
[5] Present address : Caltech Astronomy, MC105-24, Pasadena, CA 91125, USA

Received August 30, 2021

ABSTRACT

We present the first results of our deep survey of lensing clusters aimed at constraining the abundance of star-forming galaxies at $z \sim 6-10$, using lensing magnification to improve the search efficiency and subsequent spectroscopic studies. Deep near-IR photometry of two lensing clusters (A1835 and AC114) was obtained with ISAAC/VLT. These images, combined with existing data in the optical bands including HST images, were used to select very high redshift candidates at $z \gtrsim 6$ among the optical-dropouts. Photometric selection criteria have been defined based on the well-proven dropout technique, specifically tuned to target star-forming galaxies in this redshift domain.

We have identified 18(8) first and second-category optical dropouts in A1835 (AC114), detected in more than one filter up to H (Vega) ~ 23.8 (AB ~ 25.2, uncorrected for lensing). Among them, 8(5) exhibit homogeneous SEDs compatible with star-forming galaxies at $z \gtrsim 6$, and 5(1) are more likely intermediate-redshift EROs based on luminosity considerations. We have also identified a number of fainter sources in these fields fulfilling our photometric selection and located around the critical lines. We use all these data to make a first attempt at constraining the density of star-forming galaxies present at $6 \lesssim z \lesssim 10$ using lensing clusters. Magnification effects and sample incompleteness are addressed through a careful modeling of the lensing clusters. A correction was also introduced to account for the expected fraction of false-positive detections among this photometric sample. It appears that the number of candidates found in these lensing fields, corrected for magnification, incompleteness and false-positive detections, is higher than the one achieved in blank fields with similar photometric depth in the near-IR. The luminosity function derived for $z \gtrsim 6$ candidates appears compatible with that of LBGs at $z \simeq 3$, without any renormalization. The turnover observed by Bouwens et al. (2005) towards the bright end relative to the $z \sim 3$ LF is not observed in this sample. Also the upper limit for the UV SFR density at $z \sim 6-10$, integrated down to $L_{1500} = 0.3\ L^*_{z=3}$, of $\rho_\star = 7.4\ 10^{-2}$ M$_\odot$ yr^{-1} Mpc^{-3} is compatible with the usual values derived at $z \simeq 5-6$, but higher than the estimates obtained in the NICMOS Ultra Deep Field (UDF). The same holds for the upper limit of the SFR density in the $z \simeq 8-10$ interval ($\rho_\star = 1.1\ 10^{-1}$). This systematic trend towards the bright end of the LF with respect to blank fields could be due to field-to-field variance, a positive magnification bias from intermediate-redshift EROs, and/or residual contamination. Given the low S/N ratio of the high-z candidates, and the large correction factors applied to this sample, increasing the number of blank and lensing fields with ultra-deep near-IR photometry is essential to obtain more accurate constraints on the abundance of $z \gtrsim 6$ galaxies.

Key words. galaxies : formation – galaxies : high redshift – galaxies : photometry – galaxies : clusters : lensing –

1. Introduction

During the last decade considerable advances have been made in the exploration of the early Universe, from the discovery and detailed studies of redshift $z \sim 3$ galaxies (the so-called Lyman break galaxies, LBGs, e.g. Steidel et al. 2003), to $z \sim 4$–5 galaxies found from numerous deep multi-wavelength surveys, to galaxies at $z \sim 6$–7, close to what is believed to be the end of reionization epoch of the Universe (e.g. Hu et al. 2002, Kodaira et al. 2003, Cuby et

---

Send offprint requests to: Johan Richard, johan@astro.caltech.edu

* Based on observations collected at the Very Large Telescope (Antu/UT1), European Southern Observatory, Paranal, Chile (ESO Programs 69.A-0508, 70.A-0355, 271.A-5013, 272.A-5049, 73.A-0471) and the NASA/ESA *Hubble Space Telescope* obtained at the Space Telescope Science Institute, which is operated by AURA under NASA contract NAS5-26555

al. 2003, Kneib et al. 2004, Stanway et al. 2004, Bouwens et al. 2004b). Extending the searches beyond $z \simeq 6.5$ and back to ages where the Universe re-ionized (cf. Fan et al. 2002) requires extremely deep observations in the near-IR bands. Astounding depths can be reached in ultra-deep fields, as demonstrated e.g. with J and H imaging of the NICMOS Ultra-Deep Field (UDF; Thompson et al. 2005; Bouwens et al. 2004a) from which 5 faint ($H_{AB} \sim 27$) candidates at $z \sim$ 7–8 have been identified (Bouwens et al. 2004b).

On the other hand, recent `WMAP` results seem to place the first building blocks of the Universe at redshifts up to $z \sim 10-15$ (Spergel et al. 2006) and very distant star-forming systems could have been responsible for a significant part of the cosmic reionization. The end of this epoch is suggested to be at $z \sim 6.0-6.5$ from the spectrum of high redshift quasars (Fan et al. 2002). Therefore, constraining the abundance of $z > 7$ sources is an important challenge of modern cosmology.

Photometric selection of high-redshift galaxies, such as the Lyman-break technique (e.g. Steidel et al. 1995), has been successful in identifying star-forming objects at $z \sim$ 2-4 (cf. Steidel et al. 2003, Shapley et al. 2003) and up to $z \sim 6$ (Bunker et al. 2003, Mobasher et al. 2005). At redshifts $z \gtrsim 5$, only ≈ 30 galaxies are currently known with confirmed redshifts (cf. review by Spinrad 2003). For now, more than 5 galaxies with $z \sim 6.5$ (Hu et al. 2002, Kodaira et al. 2003, Cuby et al. 2003, Kneib et al. 2004) are known with secure redshifts. These objects are generally found through their Lyman-α emission which is redshifted into the $\sim$ 9200 Å window, the "reddest" window relatively free of skylines in the optical. The abundance of $z \sim 10$ galaxies was recently discussed by Bouwens et al. (2005a) using NICMOS-UDF J_{110} and H_{160} data. Their conclusion is that strong evolution exists between $z \sim 7-8$ and $z \sim 3-4$, the SFR density being much lower at very high z down to the limits of their survey ($L_{1500} = 0.3 L^*_{z=3}$). However, it is crucial to increase both the size and the depth of the surveyed field to set strong constraints on the star-formation at $z \gtrsim 7$, as field-to-field variance can be important.

In this paper we present the first results of our deep survey of lensing clusters aimed at constraining the abundance of star-forming galaxies at $z \sim 6-10$, using lensing magnification to improve the search efficiency and subsequent spectroscopic studies. The motivations are the following. On the one hand, our understanding of the first generation of stars and galaxies, the so-called Population III objects (cf. review of Loeb & Barkana 2001), has improved with the development of new models for these low-metallicity starbursts (Tumlinson & Shull 2000, Bromm et al. 2001, Schaerer 2002, Schaerer 2003). The observational properties inferred from this modeling show us that it is now possible to detect some of these objects at $z \sim 8-10$, thanks to the intensity of their emission lines, using very deep near-IR surveys on 8 m-class telescopes (e.g. Schaerer & Pelló 2001, Barton et al. 2004).

Our project is based on the photometric pre-selection of candidates making use of the natural magnification provided by foreground lensing clusters. This technique, first referred to as the "gravitational telescope" by Zwicky, has proven highly successful in identifying a large fraction of the most distant galaxies known today thanks to magnifications by typically 1–3 magnitudes (e.g. Franx et al. 1997, Ellis et al. 2001, Hu et al. 2002, Kneib et al. 2004).

We present a color-color selection similar to the Lyman-Break technique, used to identify very high redshift objects using their specific spectrophotometric properties. As first targets for our survey, we have chosen fields centered on lensing clusters with well-constrained mass distributions, and already known to be efficient gravitational telescopes. We use the sample of high-redshift candidates selected in these fields to constrain the abundance of star-forming galaxies up to $z \sim 10$.

The plan of this paper is as follows: in Sect. 2 we justify the observing strategy and the photometric criteria adopted in this project. Photometric observations and data reduction are described in detail in Sect. 3 and 4. The construction and analysis of the photometric catalogs is given in Sect. 5. The photometric selection of very high redshift candidates is presented in Sect. 6. The properties of the final list of candidates, including spectral energy distributions (hereafter SEDs), photometric redshifts and magnification estimates, are detailed in Sect. 7. In Sect. 8 we discuss the intrinsic (lens-corrected) properties of this sample, the number-density of star-forming galaxies at $z \sim 6-10$ as compared to simple model expectations, and the implications for the cosmic SFR. We also summarize our ongoing spectroscopic survey in these fields. Conclusions are given in Sect. 9. In the appendix we provide more details on the improvement of the data reduction procedure, the completeness and false-positive detection estimates in the different fields and filters, as well as additional tests performed on the reliability of optical dropouts.

Throughout this paper, we adopt the following cosmology: a flat Λ-dominated Universe with the values $\Omega_\Lambda = 0.7$, $\Omega_m = 0.3$, $\Omega_b = 0.045$, $H_0 = 70\ km\ s^{-1}\ Mpc^{-1}$, and $\sigma_8 = 0.9$. All magnitudes given in the paper are quoted in the Vega system. Conversion values between Vega and AB systems for these filters are given in Table 1.

2. Simulations and observing strategy

Our project aims to search for $z \gtrsim 6$ galaxies, typically in the $z \sim$ 7–10 domain. We have performed simulations to estimate the expected magnitudes of galaxies at such redshifts, and to establish robust photometric criteria to select high-redshift candidates behind lensing clusters. For this, we have used the evolutionary synthesis starburst models by Schaerer (2002, 2003) for Population III and extremely metal deficient galaxies, together with the usual templates available for normal galaxies. In particular, we used the empirical SEDs compiled by Coleman, Wu and Weedman (1980) to represent the local population of galaxies, with spectra extended to wavelengths $\lambda \leq 1400\,\text{Å}$ and $\lambda \geq 10000\,\text{Å}$ using the equivalent spectra from the Bruzual & Charlot GISSEL library for solar metallicity (Bruzual & Charlot 1993). We also included the starbursts templates SB1 and SB2, from Kinney et al. (1996), and the low metallicity galaxy SBS0335-052 (Izotov, 2001, private communication).

We consider a fiducial stellar mass halo of 10^7 $\mathrm{M}_{\odot}$, corresponding to a collapsing DM halo of 2×10^8 $\mathrm{M}_{\odot}$. With a ΛCDM model and the cosmological parameters adopted here, we expect ~ 10 of such DM haloes per Mpc^3 within the relevant redshift range $z \sim 5-10$, and ~ 1 Mpc^{-3} with a DM halo of 10^9 $\mathrm{M}_{\odot}$ (e.g. Loeb & Barkana 2001). The virial radius is of the order of a few kpc, and thus we consider that sources are unresolved on a 0.3" scale, with spherical symmetry. The reionization redshift is assumed to be $z \sim 6$, but results discussed below are independent of this precise value. Lyman series troughs (Haiman & Loeb 1999), and Lyman forest absorptions following the prescription of Madau (1995) are included. Although a detailed description of Lyman-α emission is out of the scope of this paper, we have taken into account the possible impact of the main emission lines on the integrated colors using rather simple and extreme assumptions. Simulations accounting for an extended Lyman-α halo (cf. Loeb & Rybicki 1999) have been computed, together with a simple parametrization of the fraction of Lyman-α flux entering the integration aperture. Two extreme assumptions are considered here for the IMF, either a standard Salpeter IMF, with stars forming between 1 and 100 $\mathrm{M}_{\odot}$, or a top-heavy IMF, with stellar masses ranging between 50 and 500 $\mathrm{M}_{\odot}$. Some preliminary versions of these simulations were presented in Schaerer & Pelló (2001) and Pelló & Schaerer (2002). Figure 1 shows, for each IMF, the expected SED of a 10^7 $\mathrm{M}_{\odot}$ stellar mass halo, using two different assumptions for age.

Nebular continuous emission and strong emission lines could have important effects on the integrated fluxes and colors of such galaxies, although broad-band colors alone do not allow one to precisely constrain the physical properties of these galaxies. The main signatures of genuine star-forming sources at $z > 6$ are common to all models: they are optical dropouts, displaying a strong break and "red" optical vs. IR colors, whereas they exhibit a "blue" SED longward of Ly-α provided reddening is sufficiently small. Different redshift intervals can be defined using an appropriate set of near-IR filters in combination with optical data. This particular application of the Lyman break technique as a function of redshift is shown in Figs. 2 to 4, for the different redshift intervals considered in this paper. For clarity, only a reduced number of models is presented in these figures. Color shifts corresponding to an intrinsic extinction of $A_V = 1$ (Calzetti et al. 2000) are shown by arrows, for starbursts at $z = 1$ and $z = 3$. Stellar colors presented in these diagrams were computed from the library of Pickles (1998).

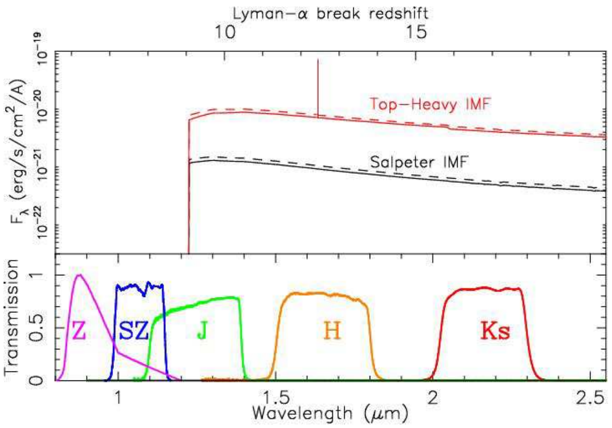

Fig. 1. Examples of SED for Pop III models used in Fig. 5 and Fig. 6 (upper panel), for a fiducial 10^7 $\mathrm{M}_{\odot}$ burst at $z = 9$, with ages 10^4 and 10^6 yrs (solid and dashed lines), and two IMF (normal Salpeter -black- and top-heavy -red-), compared to the transmission curves of the FORS/ISAAC filters set used in this survey (lower panel). The top axis gives the corresponding redshift at the wavelength of the Lyman-α break. We overplot the location of the HeII 1640 emission line (without scaling its flux), which has a small impact on the k-correction as shown in Figs. 5 and Fig. 6. Different assumptions were considered for the Lyman-α emission.

Figure 2 displays the $J-H$ versus $H-Ks$ color-color diagram for different extreme Population III starbursts within the $5 \leq z \leq 11$ interval, compared to the location of stars and normal galaxies at different redshifts. This diagram is particularly well suited to identify galaxy candidates in the $8 \leq z \leq 11$ interval among the optical dropouts. At redshifts above ~ 10, galaxies are not detected in the J band (see also Fig. 5). For galaxies at $6 \leq z \leq 9$, the same photometric selection can be performed including the z (0.9 μm) and SZ (1.1 μm) filters (Fig. 3 and 4). The characteristics of these filters are summarized in Table 1 and Fig. 1.

Once the color-selection is well established, an important issue is the photometric depth needed to detect typical stellar haloes up to a given mass, in order to derive statistically significant results on the nature and properties of $z > 6$ sources.

According to our simulations, the predicted magnitudes in the Vega system for a reference stellar halo mass of 10^7 $\mathrm{M}_{\odot}$, zero metallicity stars, a top-heavy Salpeter IMF, and a starburst younger than 10^6 yrs, typically range between ~ 24.5 and 26.0 in J in the relevant redshift range ($z \leq 8$), ~ 24.5 and 25.5 in H, and ~ 24 to 25 in Ks ($z \lesssim 10$), depending on models, within the $z \sim 6-10$ interval (see Fig. 5). For the same models, SZ and z range between $\sim 25-26$, for $z \leq 7$ and $z \leq 6$ respectively, and sources become dropouts in these filters beyond these redshifts (see Fig. 6 and Fig. 1). For a standard Salpeter IMF (from 1–100 $M_{\odot}$) these values are ~ 2 magnitudes fainter than for a top-heavy IMF; increasing the metallicity for this IMF implies a somewhat larger UV restframe flux (up to 0.5 mag brighter for solar metallicity; cf. Schaerer 2003,

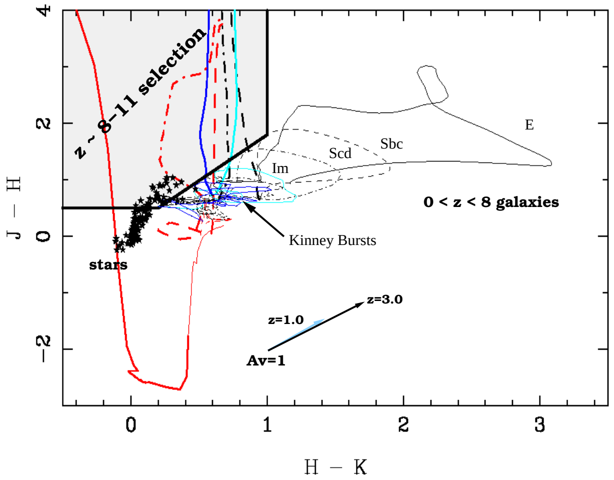

Fig. 2. J dropout selection in the $z \sim$ 8-11 domain. $J-H$ versus $H-Ks$ color-color diagram (Vega system) showing the position expected for different objects over the interval $z \sim 0$ to 11. The position of stars and normal galaxies up to $z \leq 8$ are shown, as well as the shift direction induced by $A_V = 1$ magnitude extinction. Thin and thick lines display models below and above $z = 8$. Several models for Pop III starbursts are presented, for different fractions of Lyman-α emission flux entering the integration aperture: 100% (red solid line), 50% (red dashed line) and 0% (red dot-dashed line). The location of Kinney et al. (1996) starbursts templates is also given for comparison (SB1(cyan) and SB2 (blue)). All star-forming models enter the high-z candidate region at $z \geq 8$.

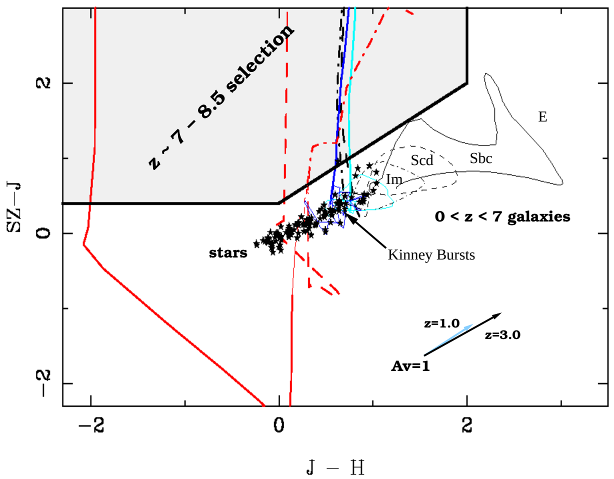

Fig. 3. SZ dropout selection in the $z \sim$ 7-8.5 domain. $SZ-J$ versus $J-H$ color-color diagram (Vega system) showing the position expected for different objects over the interval of $z \sim 0$ to 8.5. Thin and thick lines display models below and above $z = 7$ respectively. Models displayed and general comments are the same as in Fig. 2. The position of stars and normal galaxies up to $z \leq 7$ are shown.

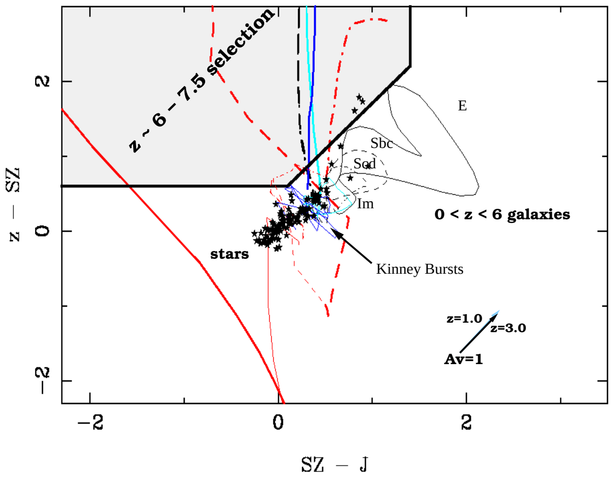

Fig. 4. z dropout selection in the $z \sim$ 6-7.5 domain. $z-SZ$ versus $SZ-J$ color-color diagram (Vega system) showing the position expected for different objects over the interval of $z \sim 0$ to 7.5. Thin and thick lines display models below and above $z = 6$ respectively. Models displayed and general comments are the same as in Fig. 2. The position of stars and normal galaxies up to $z \leq 6$ are shown.

Fig. 2). Also, obviously these magnitudes scale with stellar mass. In other words, a stellar halo with a standard IMF exhibits about the same magnitudes as a top-heavy IMF which is a factor of 10 less massive, all the other parameters being the same. This comment not only stands for PopIII models, but also for solar metallicity starbursts and constant star-forming models with standard IMF and metallicity.

Assuming a minimum gravitational magnification of $\sim$1 magnitude, if we intend to detect stellar haloes up to 10^8 $M_\odot$ (or a few 10^7 $M_\odot$, depending on IMF), the photometric depth required is of the order of $H \sim 24.0$ and $Ks \sim 23.5$ for a positive detection, and up to ~ 26.0 in z, SZ and J to identify significant dropout sources in these filters. The number of sources expected can be roughly estimated as follows. Taking into account the typical covolume surveyed in a lensing cluster under these conditions [1], the relevant density of DM haloes assuming a conservative fraction of 10% of baryonic mass converted into stars before $z = 6$ (~ 0.1 Mpc^3, corresponding to 10^{10} $M_\odot$ DM halo), and the probability of detection related to the visibility of the starburst within the relevant redshift interval (10^6 yrs restframe, thus a *duty-cycle* factor ~ 0.1 to a few 0.01; see Sect. 8), the number of sources expected ranges between a few tens and a few hundreds. We still expect a few positive detections at $z = 6-10$ with a completeness level of the order of 10% or even lower. However, strong lensing effects have to be carefully taken into account in this survey, as explained below. A detailed comparison between the number of sources expected and the number of

---

[1] a few 10^4 Mpc^3 between $z = 6$ and 10, for a $\sim 2\times2$ arcmin^2 field of view, after correction for a typical magnification factor of ~ 2

sources actually detected in our lensing fields is provided in Sect. 8.

3. Photometric data

Two lensing clusters were selected for this pilot study with the VLT: AC114 (α=22:58:48.26 δ=−34:48:08.3 J2000, $z=0.312$) and Abell 1835 (α=14:01:02.08 δ=+02:52:42.9 J2000, $z = 0.252$). AC114 is a well-known "gravitational telescope", for which multiwavelength observations are available. The corresponding lens model is well-constrained by a large number of multiple-images spectroscopically identified at high redshift (Smail et al. 1995, Natarajan et al. 1998, Campusano et al. 2001, Lemoine-Busserolle et al. 2003). Its Einstein radius is about 30″ for $z > 6$. Abell 1835 is the most X-ray luminous cluster in the *XBACS* sample (*X-ray-Brightest Abell-type Clusters of galaxies*, Ebeling et al. 1998), thus potentially one of the most efficient gravitational telescopes. Indeed, strongly lensed features were identified in this cluster, based on deep ground-based and *HST* images, and it was used to search for bright submm galaxies with SCUBA (Smail et al. 1999, Ivison et al. 2000). The mass model used is similar to the one developed by Smith et al. (2005), and gives an Einstein radius of $\sim 40''$ at high z.

We observed these clusters with ISAAC and FORS in the near-infrared domain (~ 0.9 to $2.2\ \mu$m) between September 2002 and April 2004, covering as far as possible the z, SZ, J, H, and K bands. Transmission curves for these filters are presented in figure 1. In addition, optical images at shorter wavelengths (from U to I band) are available in our group from previous surveys, or from archival data. Table 1 summarizes the main characteristics of the photometric dataset.

Note that in the remainder of the paper we shall loosely use the term "near-IR" for the SZ, J, H, and K filters, whereas "optical" refers to all filters shortwards of 1.0 μm, from U to I (or z-band when available).

3.1. Near-IR photometric observations

We obtained imaging data with the Infrared Spectrometer And Array Camera (ISAAC, Moorwood 1997) located on the Nasmyth-B focus of the 8.2m VLT-UT1 (Antu telescope), using the Short-Wavelength channel of the instrument (Cuby et al. 2000). The field of view of the camera is about 2.5 arcmin × 2.5 arcmin with a pixel size of 0.148″. The data for AC114 were acquired during UT 2002 August 19-20-22 (period 69). Due to technical problems with the instrument in this period, the usual ISAAC detector was changed for the Aladdin 1024 × 1024 InSb array. The data for Abell 1835 were acquired during UT 2003 January 14, February 9-11-12-14-15 (period 70, JHK), and UT 2004 April 20 and May 15 (period 73, SZ) with the usual Hawaii Rockwell 1024 × 1024 Hg:Cd:Te Array. Differences in efficiency between these two detectors have been re-

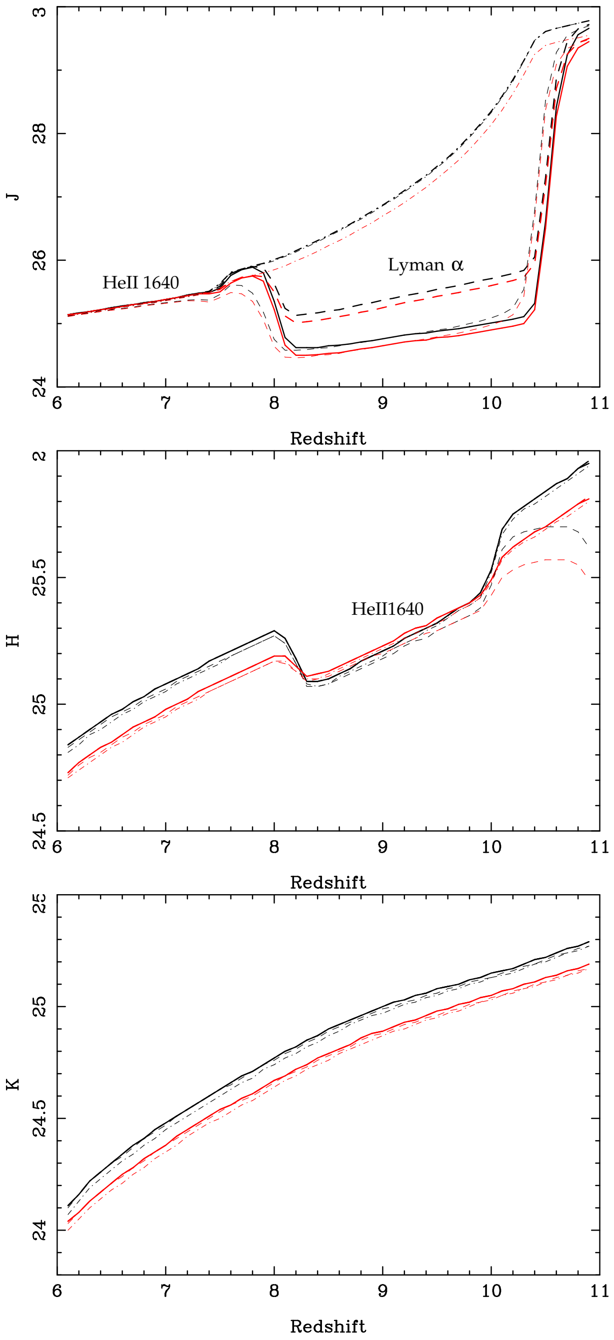

Fig. 5. From top to bottom, J, H and Ks magnitudes as a function of redshift for a top-heavy IMF, for a fiducial stellar halo of 10^7 M$_\odot$. The values corresponding to a normal Salpeter IMF are about 2 magnitudes fainter over all the redshift interval. Black and red lines correspond respectively to burst ages 10^6 and 10^4 yrs. Various models for Pop III objects are presented, for different fractions of the Lyman-α emission entering the integration aperture: 0 % (thick dot-dashed line), 50 % (thick dashed line), and 100 % (thick solid line). Thin dot-dashed lines correspond to a self-consistent extended Lyman-α halo emission (Loeb & Rybicki 1999), whereas thin dashed lines display the same model with 100 % of Lyman-α emission entering the integration aperture.

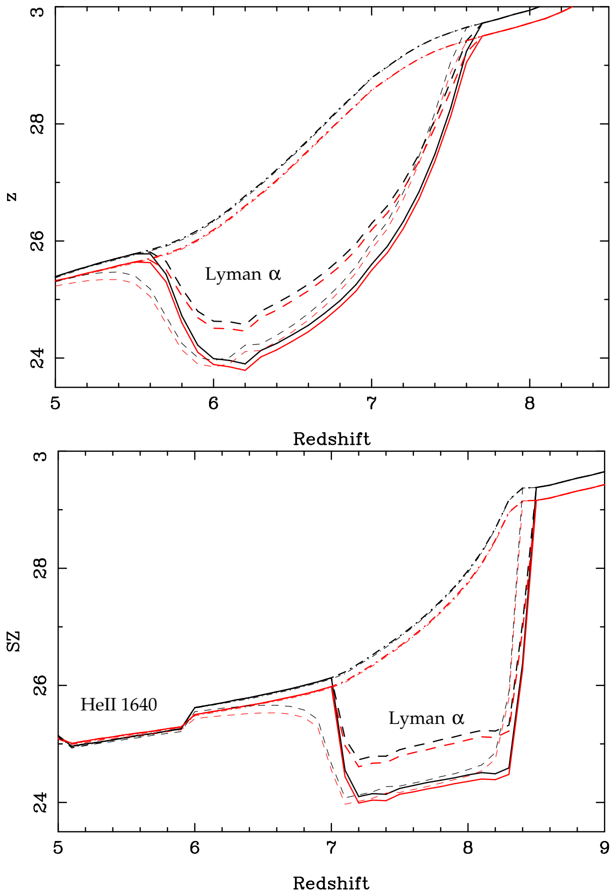

Fig. 6. From top to bottom, z and SZ magnitudes as a function of redshift, for a fiducial stellar halo of 10^7 $M_\odot$ and the same models as in Fig. 5.

ported, the Hawaii Rockwell detector providing better results in terms of photometric accuracy. [2]

Near infrared imaging is challenging because of the dominant and variable sky background. We used dithering of short exposures with subintegration × integration times of 4 × 45 s in the SZ and J bands, 11 × 12 s in the H band, and 6 × 15 s in the Ks band, with a 30″ jitter box. These values provided a good compromise between an optimal photometric depth over a large fraction of the field of view, and good sky-subtraction in a crowded field. For Abell 1835, the field center was chosen such as to prevent contamination by a very bright star located at the north of the cluster. Therefore the brightest cluster galaxy is not at the center of the field (see Fig. 10).

Calibration data were obtained in the usual way (detector darks, twilight flats, ...). Standard stars from the LCO/Palomar NICMOS list (Persson et al. 1998) were used for photometric calibration.

3.2. Optical and intermediate band images

z band observations of Abell 1835 were obtained during UT 2004 March 26 and April 10 with the FOcal Reducer/low dispersion Spectrograph (FORS2) at VLT. This instrument has a 0.252″ pixel size and a field of view of 7.2 arcmin × 7.2 arcmin. We used dithered individual exposures of 120 s.

To be able to distinguish between "low" ($z \lesssim 6$) and "high" ($z > 6$) redshift objects, we have compiled the available optical images for the two lensing clusters. For AC114, we used the data from Campusano et al. (2001) covering U to I filters, including a mosaic of deep HST/WFPC2-F702W (R) observations. Images in this band were obtained in both *high-sky* and *low-sky* modes, with different orientations on the sky, in such a way that the final composite image in this filter exhibits three regions with different behavior (noise properties, photometric depth) across the ISAAC field of view. Each of them is presented separately in Table 1.

Optical data for Abell 1835 include $BVRI$ imaging obtained with the CFH12k camera at CHFT, and HST/WFPC2-F702W (R) images acquired in *low sky* mode. Because of the field centering chosen for the near-infrared data, only half of the ISAAC field of view is covered by the HST/WFPC2 image.

For the two clusters, all optical data fully cover the relevant region studied around the cluster center. The entire ISAAC field is covered in most cases. The overlap fraction between the optical images and the near-IR data is indicated in Table 1, where the references and main properties of the data set are summarized. Overlap fractions refer to the ISAAC field.

4. Data reduction and calibration

Near infrared photometry of extremely faint sources requires a careful data reduction. The general procedure described here was performed for all the ISAAC data (SZ, J, H and Ks bands). A number of specific improvements are given with more details in App. A. For the FORS2 (z band) data, we used a standard flat-field correction and combination of the individual frames with bad-pixel rejection.

We reduced our data using IRAF procedures and according to the ISAAC Data Reduction Guide v.1.5[3]. The different steps are the following: photometric calibration, bias subtraction, flat-fielding, sky subtraction, registration and combination of the images. The reduction recipe we used, as well as some of the improvements, were mostly inspired from the reduction of near-IR observations on the HDFS field with the same instrument (Labbé et al. 2003).

Photometric zero-points were derived from LCO/Palomar NICMOS standard stars (Persson et al. 1998), observed each night using a five-point jitter pattern. After subtracting from each image the median

---

[2] For more details see Section 1.2.2 of the ISAAC user manual (Cuby et al. 2002)

[3] See `http://www.eso.org/instruments/isaac/drg/html/drg.html`

Table 1. Main properties of the photometric dataset used in this paper: filter identification, total exposure time, average seeing measured on the original images, pixel size, 1 σ limiting magnitude inside a 1.5 $''$ diameter aperture, filter effective wavelength, AB correction, overlap fraction relative to the ISAAC frames (covering an area of 2.5 arcmin × 2.5 arcmin), and references. Exposure time values of three different subsets of the HST-R_{702W} image, annotated $R_{702}^{1,2,3}$ are converted into *low sky* mode for comparison (see text for details). AB corrections (C_{AB}) correspond to $m_{AB} = m_{Vega} + C_{AB}$.

Filter	t_{exp} [ksec]	seeing [$''$]	pix [$''$]	depth [mag]	λ_{eff} [nm]	C_{AB} [mag]	overlap [%]	Reference
AC114								
U	20.00	1.3	0.36	29.1	365	0.693	43.1	Barger et al. 1996
B	9.00	1.2	0.39	29.0	443	-0.064	100.0	Couch et al. 2001
V	21.60	1.1	0.47	28.5	547	0.022	76.6	Smail et al. 1991
R_{702}^{1}	$\geq$ 8.30	0.13	0.100	$\geq$ 27.7	700	0.299	84.9	Natarajan et al. 1998
R_{702}^{2}	$\geq$ 24.90	0.13	0.100	$\geq$ 28.4	700	0.299	41.4	Natarajan et al. 1998
R_{702}^{3}	40.00	0.13	0.100	28.6	700	0.299	17.0	Natarajan et al. 1998
I_{814}	20.70	0.3	0.100	26.8	801	0.439	77.6	Smail et al. 1991
J	6.48	0.52	0.148	25.5	1259	0.945	100.0	This work
H	13.86	0.40	0.148	24.7	1656	1.412	100.0	This work
Ks	18.99	0.34	0.148	24.3	2167	1.873	100.0	This work
Abell 1835								
V	3.75	0.76	0.206	28.1	543	0.018	100.0	Czoske et al. 2002
R	5.40	0.69	0.206	27.8	664	0.246	100.0	Czoske et al. 2002
R_{702}	7.50	0.12	0.100	27.7	700	0.299	45.7	Smith et al. 2005
I	4.50	0.78	0.206	26.7	817	0.462	100.0	Czoske et al. 2002
z	6.36	0.70	0.252	26.7	919	0.554	100.0	This work
SZ	21.96	0.54	0.148	26.9	1063	0.691	100.0	This work
J	6.48	0.65	0.148	25.6	1259	0.945	100.0	This work
H	13.86	0.50	0.148	24.7	1656	1.412	100.0	This work
Ks	18.99	0.38	0.148	24.7	2167	1.873	100.0	This work

sky of all the pattern, we measured the total counts in a 20 pixel radius circular aperture, and from these integrated fluxes we derived the zero-points. Airmass differences between science exposures were corrected to a reference value for each filter using a linear relation between zero-point and airmass derived from standards stars observed at different airmasses.

After removing the instrumental ghost, substracting a median dark frame and flat-fielding our data, we used the IRAF package XDIMSUM[4] to apply a two-step sky-subtraction. During the first pass, each image is sky-subtracted using the sky pattern obtained from a group of adjacent frames and a bad pixel mask is created in the process. The relative shifts between images are derived from the position of several stars matched in each frame. Then, images are registered and combined using integer shifts values to preserve the noise properties and rejecting all bad pixels. Bright sources are detected in order to create an object mask, and a second sky-subtraction is applied to the data, this time using the mask to reject pixels located on objects in the evaluation of the sky. This improves the quality of the final stacked image.

As a cross-check for our stacking procedure, we produced another version of the final images using a slightly different reduction recipe. After the usual ghost and dark removals, we flat-fielded each image using a sky flat, created by evaluating the sky in a group of adjacent frames, again masking the bright objects. Then individual frames were registered and coadded in a standard way. The resulting images are found to be similar, in terms of quality, detection level and photometric depth, to the general procedure described above. The main difference is an enhanced quality around the bright galaxy haloes close to the cluster core, and thus we finally adopted the two-step sky-subtraction procedure.

5. Analysis of images

Since we use imaging data acquired with very different filters and instruments, we had to match them to a common reference when measuring the required multi-band photometry. However, the registration and seeing matching process generates the resampling of data, and therefore modifies the noise properties of the background in the sense that the error bars measured on these modified images by the standard means tend to be underestimated. For this reason, we preferred to use the original images to derive the error bars in each band, as explained below.

---

[4] XDIMSUM is a modified version by the IRAF group of the Deep Infrared Mosaicing Software package by P. Eisenhardt et al. See ftp://iraf.noao.edu/extern-v212/xdimsum for details

5.1. Image registration and astrometry

We registered the final SZ, J, H,and Ks band images for each cluster with a simple shift, except in the case of AC114, where we corrected for a slight distortion that appeared in the J band image.

In order to measure relative photometry in the near-IR bands, we matched all the images to a common seeing using a simple Gaussian convolution, the worst case being the J band for both clusters.

As all the photometric high-z candidates are expected to be detected in the H band we have defined an H band selected sample. The detection images were created with the original H band images, weighted by the square root of the corresponding exposure time maps in order to get a uniform background noise across the field.

The available optical images for each cluster were registered to the ISAAC combined images, using standard IRAF procedures for rotation, magnification and resampling of the data. These images were mainly used to exclude well-detected low-z sources, and also for the first visual inspection of the optical dropouts. However, resampling of data could produce both spurious detections and false non-detections among the faint sources. For this reason, further discussed in Sect. 6.2, we have used the *original* images instead to define our final sample of optical dropouts and we work on object coordinates.

We performed an astrometric calibration for all these images using $\sim$ 30 bright unsaturated objects present in the USNO catalog (USNO A2.0, Monet et al. 1998). The error obtained in the absolute astrometric calibration is typically $\sim 0.2''$ for a whole ISAAC field of view.

5.2. Photometry

We used the *SExtractor* package version 2.2.2 (Bertin & Arnouts 1996) to detect objects and to compute magnitudes within our images. We optimized the parameters to detect very faint unresolved sources. Magnitudes were measured within identical circular apertures in all filters (from optical to near-infrared), with the *SExtractor* "double-image" mode, using the H band detection images described in Sect. 5.1. Near infrared images were seeing-matched to the J band ($0.52''$or $0.65''$, see Table 1), but the seeing measured on ground-based optical bands is worse. Since optical images were only used here for non-detection purposes (i.e., for the identification of optical dropouts), we preferred to keep their original seeing instead of degrading the quality of near-IR and HST images.

SExtractor detection parameters were the following: 4 connected pixels above a threshold of 1 σ *on the detection image*, which corresponds to a central value of about 4.5 σ for a seeing-limited source, where σ stands for the typical local background noise. Magnitudes were measured within a $1.5''$-diameter aperture (i.e., 10 pixels on the ISAAC images). This value is an optimized compromise allowing us to obtain a fair estimate of the total magnitude for point-like sources on near-IR images, while keeping a good S/N on the optical images with the worst seeing ($\sim 1''$). We have also checked that magnitudes and error-bars measured within a 12 pixels ($1.7''$) diameter aperture are usually consistent within 1σ error bars for the faintest sources considered in this study.

Since *SExtractor* uses the registered, seeing-matched images to compute the photometric errors in all bands, these values are systematically too optimistic, thus leading to artificially high S/N determinations. To get more realistic errors in our photometry, we preferred an empirical method to derive them. We measured the typical RMS in the pixel distribution within apertures of the same physical size as for flux measurements: we averaged the pixel to pixel statistics in about 5000 non-overlapping apertures, randomly thrown inside regions free of objects in each original (unregistered, unconvolved) image. For each entry in the *SExtractor* output catalog, we recomputed the photometric error using the value of σ derived from these simulations. This photometric error measured in the original images was also used to compute the limiting magnitude in each band, reported in Table 1. All S/N values reported throughout the paper refer to these mock simulations.

The final catalogs include photometry within $1.5''$ aperture for all objects detected in the H band; we were able to measure photometry of very faint sources ($J \sim 24.4-24.8$, H and $Ks \sim 23.5$) with a relatively good accuracy (S/N $\gtrsim$ 3 – 4). The effective exposure time towards the edges of the field is smaller than in the central region due to the dithering pattern used in near-IR images, thus leading to brighter detection limits and an increasing number of spurious detections at the edges of the frame. In this study, we use only the region of the field for which the effective exposure time is above 50 % of the (maximum) total value. The overlap fractions relative to the ISAAC frames given in Table 1 refer to these central regions, corresponding to 6.34 arcmin^2 for Abell 1835 and 6.10 arcmin^2 for AC114. The images shown in Fig. 10 and 11 also refer to these central regions.

5.3. Photometric completeness

The characteristics of the final processed images are presented in Table 1. The seeing was measured on the original co-added images. We have computed the completeness values for point-sources, in each cluster and band, for near-IR magnitudes within the relevant intervals. These limits were obtained from direct simulations as follows. Artificial stars (i.e., seeing limited sources) of fixed magnitude, ranging between 21 and 25, were added 1000 times at 30 different random locations on our images, and then extracted using the same method for detection and photometry as for astronomical sources (described above). Only "free" sky regions were used for this exercise, with uniform noise properties. This excludes in particular the cluster core and the edges of the images, where the effective exposure time is less than 50 %. Completeness values are derived from the fraction of objects we recovered in our images. The corresponding curves are shown in Fig. 7 and the completeness levels are reported in Table 2. A completeness level of $\sim 20-30\%$ is achieved for H and $Ks \sim 23$, thus in good agreement with the requirements given in Sect. 2 for at least a few positive detections at $z \sim 6-10$.

Table 2. 90 % and 50 % completeness limits for each cluster and band, corresponding to simulations shown in Fig. 7

Cluster	Band	90 % compl.	50 % compl.
AC114	J	23.5	23.9
AC114	H	22.5	22.8
AC114	Ks	22.4	22.8
Abell 1835	z	23.0	23.6
Abell 1835	SZ	24.0	24.4
Abell 1835	J	23.3	23.6
Abell 1835	H	22.3	22.7
Abell 1835	Ks	22.1	22.7

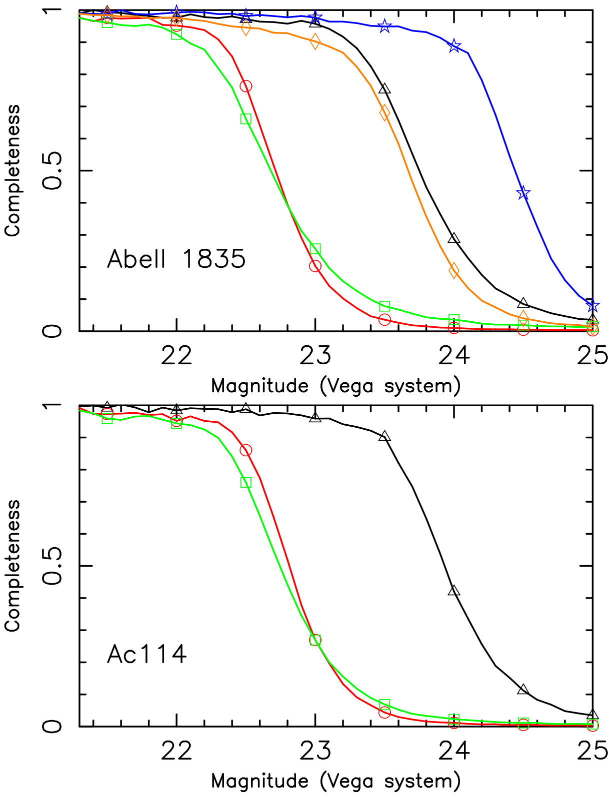

Fig. 7. Completeness curves obtained from simulations in each cluster, for the z band (orange diamonds), SZ band (blue stars), J band (black triangles), H band (red circles) and Ks band (green squares).

Our near-IR survey has reached $SZ \sim 25.6$, $J \sim 24.3$-24.4, $H \sim 23.5$ and $Ks \sim 23.1$ (AC114) to 23.5 (Abell 1835) (3 σ detection level within 1.5″ aperture), i.e. AB$\sim$ 25-25.5 in $JHKs$ and AB$\sim$26.3 in SZ. The *minimum* magnification factor over the region covered by our near-IR survey is ~ 0.7 magnitudes, and at least ~ 1 magnitude over 50 % of the ISAAC field of view. Thus, the *effective* 3σ limiting magnitudes reached here are close or similar to those attained in the HDFS (Labbé et al. 2003) in $JHKs$ (respectively AB$\sim$ 26.8, 26.2 and 26.2). Note that the limiting Vega magnitudes given in Table 1 correspond to 1σ values. Our 3σ limiting magnitudes in the H band also comeclose to the magnitudes of the $z \sim 7-8$ z-dropouts detected by Bouwens et al. (2004b) in the Hubble Ultra Deep Field, with $H_{160}(AB) \sim 26.0$ to 27.3, after correction for a typical magnification factor of at least ~ 1 magnitude.

We determine below the additional correction for incompleteness generated by our sample selection procedure. Lensing models were used to derive the effective completeness of our sample as a function of redshift and magnitude, as compared to blank fields.

6. Selection of high-z photometric candidates

This Section presents the procedure adopted to select the sample of high-redshift candidates. As described in the observing strategy (Sect. 2), color-color diagrams of optical dropouts have been used to select high-redshift candidates from our deep near-infrared images. For a subsample of them, individual probability distributions and photometric redshifts can be reliably derived from their photometric SEDs, as discussed in Sect. 7. The location of the photometric candidates with respect to the critical lines, and thus the typical magnification factors reached by our sample, are also briefly described.

6.1. Near-IR color-color diagrams of bright objects

As an additional test of the photometric selection of sources, we have checked that magnitudes and colors of bright sources ($H < 22.5$, i.e. S/N $\gtrsim$ $8-10$) are in good agreement with expectations. We have already secured the colors of cluster members during the photometric calibration described in Appendix A. Stars morphologically identified by *SExtractor* ($flag_* > 0.95$) are located at the expected position in these diagrams. A representative example is given in Fig. 8 for Abell 1835. This diagram is to be compared to the theoretical expectations displayed in Fig. 2.

If we adopt the ($R-Ks > 5.6$) definition from Daddi et al. (2000) to select Extremely Red Objects (hereafter EROs) from this sample of bright sources, we find that a few of them lie inside the low-redshift region of the diagram for each cluster, a location mainly compatible with dust-reddened starbursts. This diagram also shows that only very few *bright* objects correspond to our color-selection criteria for high redshift galaxies. All these objects are detected in the optical bands. We have carefully inspected the morphology of these sources on the HST images and found two cases: either they clearly correspond to two blended objects, or they are point-like sources. In the first case, the two objects merge in a single source on the near-IR images, in which case the photometric mea-

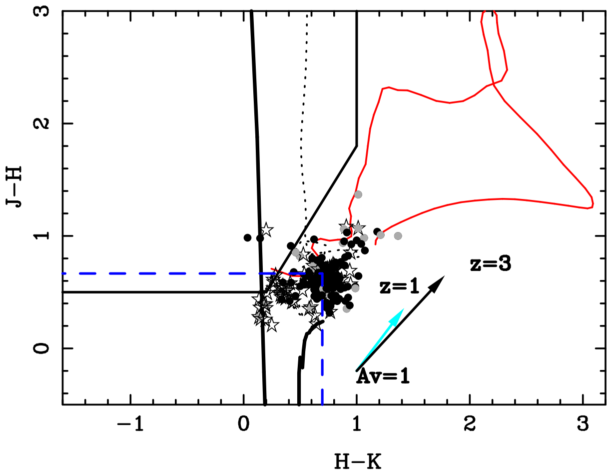

Fig. 8. Location of objects brighter than $H = 22.5$ in the $J-H$ vs $H-Ks$ color-color diagram for Abell 1835 (black dots). Special symbols are used for *SExtractor* stars ($flag_* > 0.95$, open stars) and EROs (grey dots). Predicted colors for an elliptical cluster galaxy are shown with dashed lines, and the direction of reddening is indicated by an arrow. Evolutionary tracks are overplotted as in Fig. 2, to facilitate the comparison: E galaxy (red solid line), a low-metallicity starburst (thick solid black line) and a local starburst from Kinney et al. 1996 (dotted line). Error bars are typically ≤ 0.1 mags for these objects.

surements are contaminated. In the latter case, we found stars close to saturation in one or several filters. Thus, except for these understandable cases, no bright objects ($H < 22.5$) are found to fulfill our two color selection criteria.

6.2. Catalog of optical dropouts

Optical dropouts are defined as objects non-detected in all the available optical images, from the U band to the z band. A source is considered as non-detected in a given band when its magnitude corresponds to a flux below the 1σ detection level within a $1.5''$ aperture. These are the magnitude limits reported in Table 1, also used in all tables and figures through the paper to derive limits in color.

In the first step, we used *SExtractor* in "double-image" mode, with the H band detection images described above as a reference (see Sect. 5.1). We cross-checked the detection (or non-detection) of sources on their original images, before any geometric correction or resampling. Positions for all the sources detected in the H band were computed in the original images using the appropriate geometrical transformations. An input catalog was created with these coordinates, used by *SExtractor* as input for the detection (or non-detection) of each object on the original image.

The automatic procedure described above provided a first catalog of optical dropouts containing 122 and 38 objects up to $H = 24.0$, in Abell 1835 and AC114 respectively. Since we detected sources with *SExtractor* at very faint limits in flux, all the optical dropouts were carefully examined to reject both spurious detections in the near-IR bands and false non-detections in the optical bands, using the original images.

Some objects in the first catalog were rejected because they were found to be located in noisy regions, close to the limits of the deep images or close to the haloes of bright galaxies. Some of them were contaminated because they lie too close to bright objects, in particular towards the cluster center. All these objects were removed from the dropout catalog either because they were more likely false detections, or because their photometry was highly contaminated. A mask was created to remove the remaining noisy regions (bright galaxies, galaxy haloes, ...) from the subsequent analysis. The region masked typically corresponds to ~ 20 % of the surface in both clusters. At the end of the visual inspection, only ~ 20 % of the original sample remains in the list.

Several dropout sources were found to be brighter in the Ks band image than in the H band. Their centroid determined by *SExtractor* on the detection H band image is, in principle, less accurate than in the Ks band, thus potentially leading to less optimal colors. There are 7 objects of this kind in Abell 1835 and 1 in AC114. We corrected the photometry and centroid positions for these objects by running *SExtractor* with the Ks band image as detection frame, keeping all other parameters unchanged.

Since photometry was obtained in *double mode*, magnitudes measured by *SExtractor* in the infrared bands could be incorrect due to flux contributions at the limits of the aperture whereas no object is clearly seen in the center. For 5 objects in Abell 1835 and 2 in AC114, a non-detection was forced after visual inspection.

We have considered that sources detected in at least two near-IR bands had more significance, since the probability of false-positive detections in two different bands decreases strongly compared to our estimates only based on the detection band (Sect. 5.3). These objects constitute our "second-category" sample. Among them, we define a "first-category" subsample including only the best-detected sources (having $\Delta m_H < 0.4$, equivalent to 2.5σ detection within the aperture). Objects clearly detected in the reference H band, after visual inspection by two different persons, but not detected in another filter, constitute the "third category" sample. The remaining ones (only detected in H band, and dubious after visual inspection), are considered as a "fourth category" sample, which is not discussed hereafter. Tables C.2 for Abell 1835 and C.3 for AC114 provide the coordinates and photometric properties for all optical-dropouts from the first, second and third-category samples. Identification numbers increase with measured H band magnitudes for a given cluster. The number of first/second/third-category dropouts for Abell 1835 and AC114 is 11/7/5 and 4/4/2 respectively. In the case of Abell 1835, the best limit for the optical non-detection is provided by the z band ($z_{AB} \gtrsim 27.3$, cf. Table 1). For AC114 the strongest non-detection criterion is in R/HST with $R_{AB} \gtrsim 28.$–28.9, depending on the source location.

Figures C.1 and C.2 display the thumbnail images of the relevant optical dropouts in Abell 1835 and AC114 respectively. For each source, the available near-IR images ($SZ\ J\ H\ Ks$ for Abell 1835 and $J\ H\ Ks$ for AC114), together with the strongest non-detection band (z for Abell 1835 and R/HST for AC114) are shown.

In order to derive global properties of the different types of candidates, we carefully estimated our sample completeness and the number of false-positive detections, as detailed in App. B. According to our results, *false-positive detections* are not expected up to $H = 23.0$, and they account for less than 30 % (typically 12% in A1835 and 25-33% in AC114) for first and second-category candidates brighter than $H = 23.3$, depending on the set of filters where an object is being detected (see Table B.1).

We also performed a number of additional tests on the reliability of optical dropouts, reported in App. C.

6.3. Third and Fourth category candidates

The manual classification of objects detected only in the reference H band into "third" and "fourth" category dropouts seems arbitrary at this point. We have used rather conservative criteria in this study to avoid the sample being dominated by false-positive detections, increasing with magnitude. However, a fraction of these rejected sources is actually real, although difficult to quantify with present data. A good example is A1835#35, a source kept as a secondary target for spectroscopy, for which we have obtained a spectroscopic confirmation of $z = 1.68$, using Hβ and [OIII]λ,λ 4959,5007 lines detected in the J band with ISAAC (see Richard et al. 2003 and discussion in Sect. 8.6). This object should have been removed from our present sample: it is marginally detected in H and K bands, and is fainter than any other object reported in Tables C.2 and C.3.

6.4. Crude redshift estimate of high-$z-$ candidates from near-IR colors

We have produced a first list of potential "high redshift" candidates by applying the color-color selection criteria described in Sect. 2 to the catalog of optical dropouts (see Fig. 9). We select objects with a fairly red color at wavelengths close to the Lyman-α break/Gunn-Peterson trough ("dropout"), and blue colors longward of it, indicative of a blue UV restframe spectrum.

In practice, depending on the available near-IR photometry, the candidates can be classified in three approximate redshift bins between 6 and 10. From the JHK color-color diagram, available for both clusters, we selected a sample of candidates in the range $8 \lesssim z \lesssim 10$. The selection region we used is defined by :

$(H-K) < 1.0$
and $(J-H) > 0.5$
and $(J-H) > 1.625\ (H-K) + 0.175.$

As shown in Fig. 9, the majority of optical dropouts in both clusters fulfill the high-z requirements. The majority of those in the remaining part of this diagram fulfill the EROs selection criterion of $R-K > 5.6$, and thus they are possible intermediate-redshift reddened starbursts.

To further distinguish the objects at $z \lesssim 8$ we use, where available, the $SZJH$ color-color diagram to select candidates in the range $7 \lesssim z \lesssim 8.5$ and the $zSZJ$ diagram in the range $6 \lesssim z \lesssim 7.5$. The selection in the $SZJH$ diagram is defined by

$(J-H) < 2.0$
and $(SZ-J) > 0.4$
and $(SZ-J) > 0.8\ (J-H) + 0.4$

In the $zSZJ$ diagram it is defined by

$(SZ-J) < 1.4$
and $(z-SZ) > 0.6$
and $(z-SZ) > 1.23\ (SZ-J) + 0.477$

Figure 9 presents the color-color diagrams for the 18 (8) first and second-category dropouts detected in Abell 1835 (AC114). We used the location in these diagrams to distribute the candidates within the different redshift ranges. For a subsample of these optical dropouts, individual photometric redshifts were derived from their photometric SEDs. The attribution of a redshift to each candidate is discussed in Sect. 7.

7. Results

We shall now present the results concerning the magnification of the high-z candidates, their SEDs and photometric redshifts. Some individual objects deserve particular discussion. We also provide some elements to understand the differences found between the two clusters.

7.1. Magnification of the high-z candidates

High-z candidates were selected based *only* on their photometric properties. Their positions with respect to the critical lines were not considered as a selection criterion. However, objects located close to the high-z critical lines are of greater interest, because of the larger magnification.

Figures 10 and 11 show the final-processed H band images used for the object detection with *SExtractor*, together with the location of our candidates in both clusters. Also plotted are the critical lines at $z = 1.5$ and $z = 10$, and contours of iso-magnification assuming a source redshift of $z = 9.$ computed from the lensing models for Abell 1835 (similar to Smith et al. 2005) and AC114 (Natarajan et al. 1998, Campusano et al. 2001). The position of these lines is weakly sensitive to source redshift within the relevant range $z \sim 6$ to 10. For a given redshift estimate, the location of the high-z candidates on the field allows us to derive their magnification factors (see Tables C.2 and

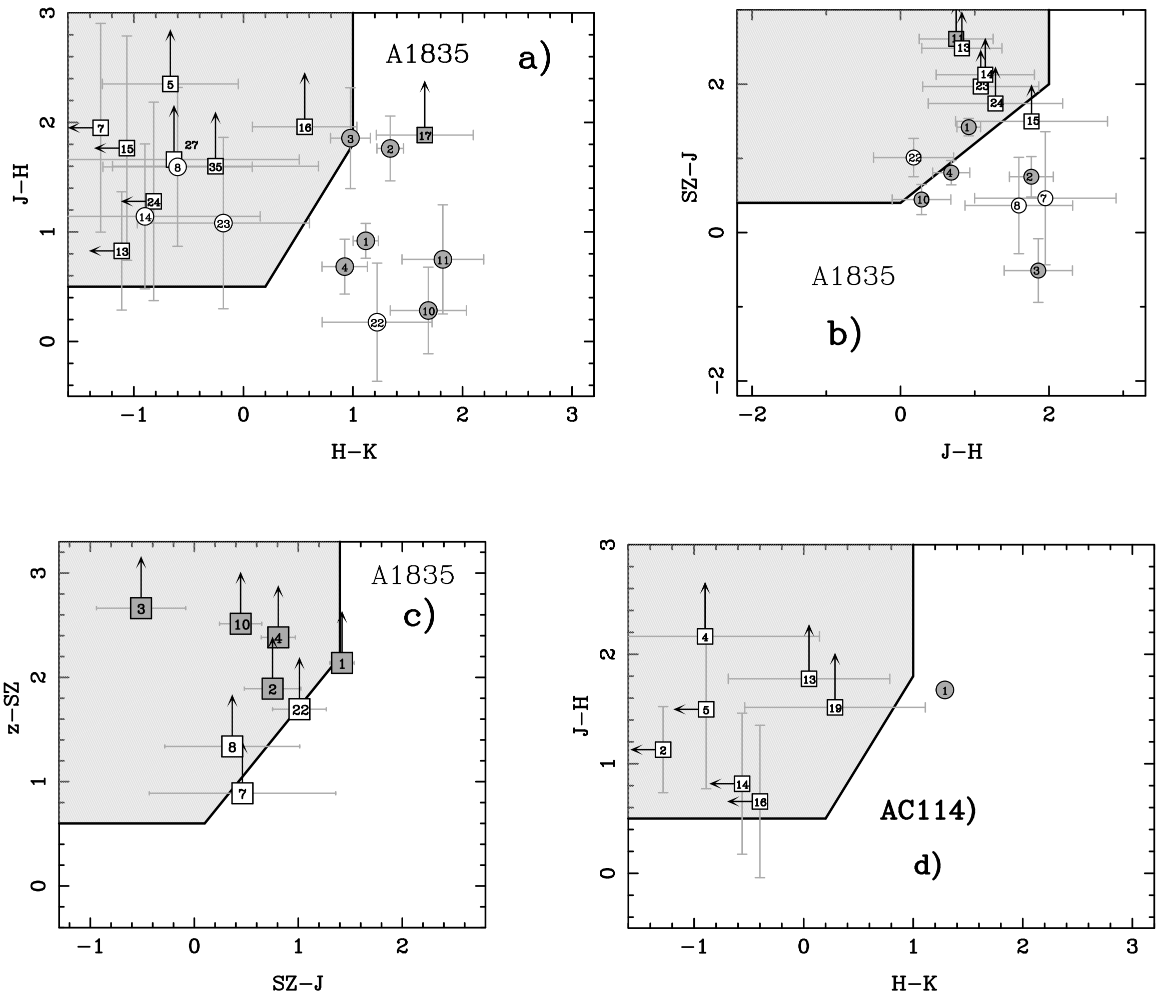

Fig. 9. Color-color diagrams showing the location of all optical-dropouts detected in Abell 1835 (a-b-c), AC114 (d), and the delimitation of the selection region used in the different redshift domains: $JHKs$ ($z \sim 8-10$), $SZJH$ ($z \sim 7-8.5$), and $zSZJ$ ($z \sim 6-7.5$) (see text). The identification numbers are indicated according to Tables C.2 and C.3. For a given diagram, circles and squares correspond to objects detected in three and two filters respectively; upper limits are displayed by an arrow. Optical dropouts fulfilling the EROs definition are shown in grey. Dropouts are all detected in the H band, and non-detected in the z band. Sources are presented in diagrams (a) and (d) if they are detected either in J or K, and in diagrams (b) and (c) if detected in J or SZ.

C.3). μ_6 and μ_{10} give the magnification factors assuming a source redshift of 6 and 10 respectively. Where applicable, the adopted magnification $\tilde{\mu}$ is computed assuming the "adopted" redshift $\tilde{z}$ described in Sect. 7.2.

The uncertainty in the magnification factor associated with the uncertainty on the redshift value is usually smaller than 10%, except for a few objects exhibiting the largest magnification factors ($\mu > 10$), i.e. located within a few arcsecs of the critical lines. Also the magnification factor at a given position on the image plane varies slowly with redshift for sources located more than $\sim 10''$ away from the critical lines. Since lensing models are mainly based on the identification of multiple images with secure spectroscopic / photometric redshifts, the uncertainty in the derived magnification factor is usually smaller close to these regions. However, it could be larger in the case of Abell 1835, because the model is based only on one multiple image system. Because of the relative insensitivity to source redshift and position on the image plane, a refined version of lensing models will not change our present results and conclusions.

For objects located close to the critical lines at high redshift, we used the same lensing models to look for possible multiple images which could affect our analysis (number counts, etc.) or allow us to better constrain the position of the critical lines at $z \gtrsim 6$. With the present data, we could not find any pair of objects that would be a fair multiple image candidate, although this possibility cannot be ruled out because of completeness considerations (see Sect. 5.3).

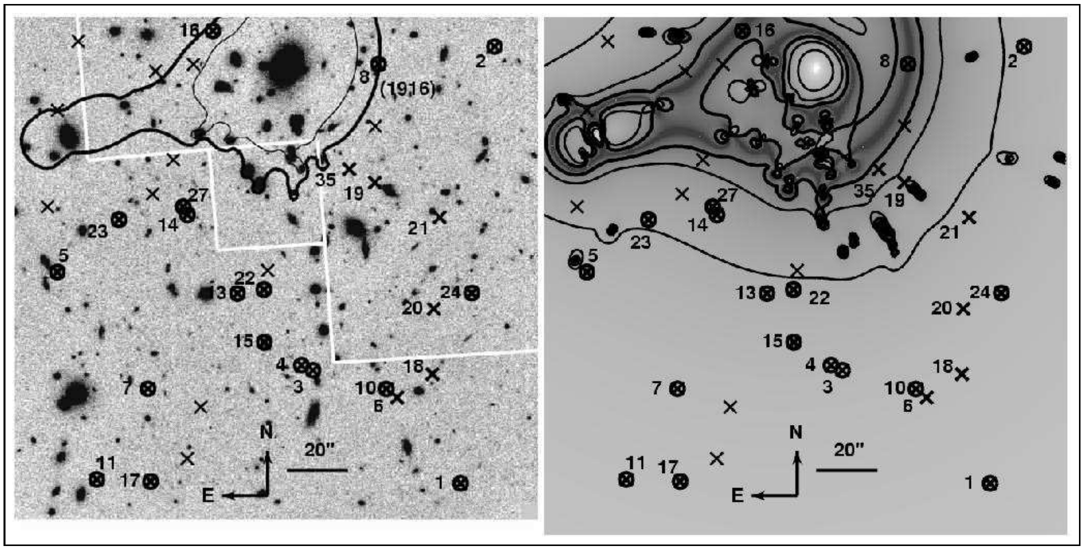

Fig. 10. Left : H band image of the lensing cluster Abell 1835 showing the location of the critical lines at $z = 1.5$ (thin solid curve) and $z = 10$ (thick solid curve). All candidates are shown with crosses; identification numbers are the same as in Table C.2. First/Second-category dropouts are circled and fourth-category objects are not labeled. Right: location of the same objects relative to the magnification across the field. Contours are overplotted for magnification values of 1, 2 and 3 magnitudes, computed assuming sources at $z = 9$, although the position of these lines is weakly sensitive to source redshift within the relevant range $z \sim 6$ to 10. White lines delimit the footprint of the R_{702} WFPC image, covering $\sim 46\%$ of the whole ISAAC field of view.

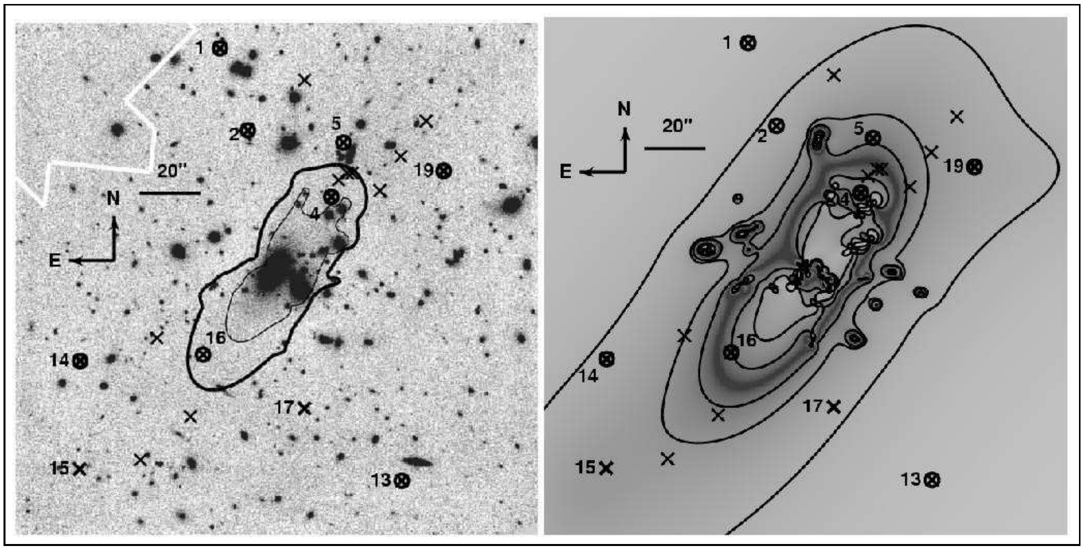

Fig. 11. Same caption as Fig. 10 for the cluster AC114. Identification numbers are the same as in Table C.3. White lines delimit the footprint of the R_{702} WFPC image, covering $\sim 85\%$ of the whole ISAAC field of view.

7.2. SED properties and photometric redshift estimates

The position of optical dropouts on the different color-color diagrams provides a first estimate of their photometric redshifts, and an objective criterion allowing us to classify them into different redshift intervals. This criterion can be refined for about 30% of our candidates presented below, for which the S/N is sufficient to derive individual probability distributions in redshift. These sources are among the brightest candidates in the H band, or have been detected in other filters with S/N$\sim 4-10$. Of particular interest are the optical dropouts which can be unambiguously excluded from the $z \gtrsim 6$ sample using photometric redshift considerations.

Probability distributions and photometric redshifts were derived for our candidates from broad-band photometry over a wide wavelength interval, using an adapted version of the public photometric redshift software *Hyperz* (Bolzonella et al. 2000). Best-fit redshifts and redshift probability distributions between $z = 0$ and 12 were computed through a standard SED fitting procedure. We used a variety of template models: starbursts (Kinney et al. 1996; SBS0335-052, Izotov 2001), evolutionary models from the GISSEL library (Bruzual & Charlot 1993), empirical templates from Coleman et al. (1980), and theoretical templates for zero metallicity (PopIII) and low metallicity starbursts (Schaerer 2003). Intrinsic reddening was considered as a free parameter ranging between $A_V = 0$ and 3 magnitudes, according to the Calzetti et al. (2000) extinction law. The Lyman forest blanketing is included following the prescription of Madau (1995). The non-detection in the optical bands was used as a constraint when computing photometric redshifts.

For further discussion on the candidates, we shall adopt a redshift value $\tilde{z}$ combining all the constraints obtained from the color-color diagrams and the photometric redshift determinations. Redshift values $\tilde{z}$ and redshift intervals adopted for each optical dropout are reported in Tables C.2 and C.3. Depending on its photometric redshift probability distribution $P(z)$, we attribute a redshift quality to each candidate (ϕ_z in Tables C.2 and C.3) as follows:

(A) Objects displaying a unique solution in their probability distribution in redshift ($P(z)$), irrespective of the redshift, with a good SED fitting for this unique solution (i.e. absolute probability higher than 90% in most cases), with no other secondary solutions with reduced χ^2 better than χ^2(best fit) + 1. The best fit redshift in this case corresponds to the $\tilde{z}$, and $z1$,$z2$ given in the tables correspond to 1σ redshift intervals (68% confidence intervals).

(B) Objects showing a degenerate solution between $z \gtrsim 6-12$ and a lower redshift solution, in general within $z \sim 1.5$–2.5. In this case, the two solutions are equally significant, with a good SED fitting in both cases (reduced $\chi^2 \lesssim 1$). We adopt in this case the higher redshift solution in a similar way as for (A).

(C) Objects for which no reliable *individual* photometric redshift solution could be obtained, either because their $P(z)$ is basically "flat", without a significant solution, or because multiple degenerate solutions exist, all of them providing a poor fit in terms of absolute probability. In this case, the redshift limits [$z1$, $z2$] and $\tilde{z}$ in the Tables correspond to the mean redshift and the redshift intervals defined by the color-color diagram selection:

[6.0-7.5] and 6.75 for $zSZJ$

[7.0-8.5] and 7.75 for $SZJH$

[8.0-10.0] and 9.0 for JHK

For objects displaying a peak at high-z in their probability distributions $P(z)$ (quality types A and B), the best-fit $\tilde{z}$ is always found as expected within the redshift interval defined by the color-color diagrams. SZ band photometry is not available for AC114, and thus we only considered the [6.0-8.0] and [8.0-10.0] redshift intervals for this cluster.

Figures C.1 and C.2 also display the SEDs and best-fit models for optical dropouts, only for first and well-detected second-category sources. Several of these objects seem too bright to be high-z sources. We discuss below these and other peculiar objects individually. A more detailed description of individual objects will be presented elsewhere.

7.3. Contamination by mid-z interlopers

Because of the large photometric errors of the selected optical dropouts in the near-infrared bands (up to ~ 0.6 magnitudes in some cases) our high redshift sample is susceptible to contamination by low redshift interlopers falling in our color-color selection regions. We derive a basic idea of this contamination factor based on the spectroscopic catalog from the HDFS (Noll et al. 2004) for which the near-infrared photometry was obtained with the same instrument and filters (Labbé et al. 2003).

Photometric errors were introduced in the HDFS catalog following a Gaussian distribution of fixed σ in each J, H and K_s band. Different values of σ were used to mimic the typical S/N in the sample of optical dropouts, and different redshift intervals were considered for the HDFS sample. The worst contamination level by mid-z interlopers on the $(J-H)$ vs $(H-K)$ color-color selection diagram ranges between 20 and 25%, depending on the redshift intervals, when applying a 0.6 mag. photometric scatter to all filters, i.e. error bars sensibly larger than those reported in Tables C.2 and C.3. None of the contaminant sources would have been selected as an optical dropout. Therefore, this source of contamination should represent a second order correction for our sample.

7.4. Individual objects in Abell 1835

Optical dropouts in this cluster are distributed as follows (cf. Table C.2, Figure C.1). We have detected 7 objects satisfying the ERO criterion. Among them, two (A1835#2 and A1835#17) are unambiguously identified as low-z sources, two display a non-standard behavior in their SED (A1835#10 and A1835#11), and one is clearly variable in (at least) the SZ band (A1835#4). In general, optical dropouts displaying anomalous SEDs as compared to young starbursts are either variable sources (A1835#4) or sources whose nature could not be determined with the present data (A1835#8, A1835#10, A1835#11). These objects, marked as "Ex." in Tables C.2 and C.3, are not considered as true high-z candidates and are therefore excluded from the high-z sample. Similar arguments can be used to remove the other two "bright" EROs (A1835#1, A1835#3) from the sample.

A general comment concerning the "bright" EROs is needed here. As mentioned above, only 2 of these in A1835 and 1 in AC114 could be identified unambiguously as intermediate-z galaxies using photometric redshift considerations. All the others are difficult to reconcile with normal "mid-z" galaxies because of their relatively blue continuum in the near-IR JHK domain, yielding solutions at $z \sim$ 6–8 which are equally likely or even better (see Fig. C.1 and Table C.2). However, they are extremely luminous if at such high-z, typically $M_B \sim -25.0$ to -26.5 for the brightest ones. Although "bright" high-z sources of this kind may exist, up to $50L_*$, as recently proposed by Mobasher et al. (2005) for their massive post-starburst galaxy at z∼6.5, we exclude these sources from the high-z sample, and consider the low-z solution as more plausible at this stage. Spectroscopic information is needed to further characterise these faint lensed EROs, and determine their nature by a measurement of their redshifts.

Some sources in A1835 deserve specific comments.

- A1835#2 : This source corresponds to J5, the near-IR counterpart of the SCUBA-selected galaxy SMMJ14009+0252 (Ivison et al. 2000, Smail et al. 2002). The near-IR photometry reported here is compatible with the recent results by Frayer et al. (2004). It satisfies the ERO criterion, and it is likely a low-z source as suggested by our SED fitting result: z=1.34 (with 1σ ranging between z=1.18 and 1.64). This solution is in good agreement with the redshift constraints $0.7 \lesssim z \lesssim 1.8$ derived from the radio-submm spectral index $\alpha_{1.4}^{850}$, but inconsistent with the range $3 \lesssim z \lesssim 5$ suggested by the submm colors (Ivison et al. 2000).
- A1835#4 : As mentioned in Appendix C, this source displays a difference of 0.4 mags in SZ (more than 3 σ) between the two series of images obtained on the 19 April and the 15 May, which seems to indicate an intrinsically variable source.
- A1835#8 : This object (previously named A1835#1916, also known as the $z \sim 10$ candidate) was studied in detail in Pelló et al. (2004ab). The photometry presented here is an improved version; the present and earlier magnitudes in the common filters are compatible within 1σ error-bars. The field around A1835#1916 has been reobserved between 30 May and 6 June 2004 by Bremer et al. (2004) with NIRI/GEMINI in the H band. Surprisingly, the object is not redetected in these images, which are at least ~ 0.5 mag deeper than the ISAAC images taken approx. 15 months earlier. The reality of our initial photometric detections is not questioned by Bremer et al. who reconfirm it using our data, although the photometric properties of this source are still a matter of debate (Lehnert et al. 2005, Smith et al. 2006). The detection in 3 bands where the object is re-detected, including our new SZ images (see Table C.2), makes a spurious event highly unlikely (about 12% probability, from our estimates given in Table B.1). When we consider the present results together with our previous findings (the source was virtually non-detected in our J images), and the non-detection by Bremer et al. in the H band with new independent data, this source could be intrinsically variable. Its nature (and hence also its redshift) presents a puzzle, and will be discussed elsewhere. Hereafter we do not consider this source within the high-z sample.
- A1835#35 : This is a third-category candidate (previously named A1835#2582) and a rather unusual emission line galaxy already studied in detail by Richard et al. (2003). As for #8, the present and earlier magnitudes in the common filters are compatible within 1σ error-bars. The marginal detection of this object in the I and J bands reported by Richard et al. (2003) is found to be non-significant with our new and more conservative error estimates. Thanks to [OIII]$\lambda\lambda$4959,5007 and Hβ detected in the J band, #35 has been identified as an extremely faint galaxy at $z = 1.68$, with $M_B \sim -16.4$ and a gravitational magnification of ~ 2 magnitudes. This object has been removed from the photometric sample of high-z candidates.

7.5. Individual objects in AC114

From the 10 optical dropouts selected in AC114 (cf. Table C.3, Figure C.2), 8 are in the first and second-category samples. Among those, only one object satisfies the ERO criterion (AC114#1, cf. below). The lack of z and SZ photometric data for this cluster precludes a further classification into redshift bins between $z \sim 6-8$.

- AC114#1 : This source satisfies the ERO criterion, and it is likely a low-z galaxy according to our SED fitting result: $z = 1.62$ (with 1σ ranging between $z = 1.58$ and 1.89).

7.6. Differences between the two lensing fields

The total number of remaining first and second-category high-z candidates in AC114 as compared to Abell 1835 is found to be in a ratio of 7/10 (9/15 whith third-category candidates), after excluding EROs in both two clusters. Several reasons could explain this difference, in addition to field-to-field variance:

- The depth of the near-IR images is less in AC114 as compared to Abell 1835, by 0.1 and 0.4 magnitudes in J and Ks respectively. Also the overall detection image in H is noisier for AC114, as shown in Table B.1, rendering the identification and visual inspection of near-IR detections more difficult. We expect a larger fraction of (blind) false positive detections in AC114 than in Abell 1835 (Table B.1). Thus, if the sample was dominated by such detections, the number of candidates should be smaller in Abell 1835 than in AC114. However, the opposite trend is observed, which means an efficient (manual) control of the sample.
- The optical images used to identify dropouts are not identical in the two cases. In Abell 1835, the main constraint comes from a deep z band image (limiting magnitude $z_{AB} \gtrsim 27.3$, whereas it is $I_{AB} \gtrsim 27.2$ in AC114). In AC114, the strongest non-detection criterion is set by the R/HST image (limiting magnitude

$R_{AB} \gtrsim 28.7 - 28.9$ in the relevant region of the field, whereas it is $R_{AB} \gtrsim 28.0$ in Abell 1835). Star-forming *and* highly-reddened intermediate-z sources such as A1835#35 could survive more easily in the Abell 1835 sample than in AC114 because of the difference in the R band.

- Geometrical considerations coming from lensing are also to be taken into account. Abell 1835 is not centered on the CD galaxy, and the two clusters have different redshifts ($z = 0.252$ and 0.312). As shown in Fig. 10 and 11, the magnification factors across the ISAAC field of view are different thus leading to different *effective* surveys, as discussed in detail in Sect. 8. In summary, within the redshift domain considered here ($6 \lesssim z \lesssim 10$), the two clusters cover about the same area *on the sky* close to the critical lines for the largest magnifications factors beyond 5 (24 and 21% of the total surface respectively), and thus we expect (and observe) the same number of such sources in the two fields. On the contrary, for magnification factors below 5, the two clusters exhibit a different behavior: 31 and 47% of the total surface respectively for Abell 1835 and AC114, for magnifications factors between 2 and 5, and 45 and 32% of the total surface respectively for magnifications factors below 2 (0.75 magnitudes). In other words, the sample observed in Abell 1835 is expected to be dominated by sources with magnification factors below 2 (up to ∼50-60%, assuming sources with a uniform distribution in z and same luminosities, after completeness correction), whereas the majority of candidates detected in AC114 are expected to exhibit magnification factors above 2 under the same conditions. This is the qualitative behavior of candidates actually observed. For magnifications factors above 2, and taking into account that we are dealing with small number statistics, the relative number of candidates detected in both clusters is in good agreement with expectations. On the contrary, the simple considerations given here cannot explain the excess in the number of candidates detected in Abell 1835 with respect to AC114, for magnification factors below 2.

8. Discussion

In this section we discuss the implications of the present results in terms of abundance of star-forming galaxies at $6 \lesssim z \lesssim 10$. We present and discuss the intrinsic properties of candidates actually detected, after correction for lensing magnification, and we compare the observed counts with order-of-magnitude expectations obtained from simple modeling. The observed number densities of candidates, as seen through gravitational lenses, are translated into *effective* number densities through a careful modeling of lensing effects, easily comparable with blank field studies. The luminosity function and the cosmic star formation rate derived from our sample of $6 \lesssim z \lesssim 10$ candidates is also presented and discussed. The large correction factors applied to this sample make the determination of integrated quantities, such as luminosity functions and SFR densities extremely difficult. In the final section, we briefly describe the preliminary results obtained on the spectroscopic follow-up of the photometric candidates.

8.1. Intrinsic properties

The typical magnification values of our candidates range between 1.5 (∼ 0.44 mags) and 10 (2.5 mags). For some objects very close to the critical lines, we found magnification values $\mu > 25$. However, because of the underlying error in the precise location of the critical lines from the models, we prefer to adopt a more conservative lower limit of $\mu = 25$ for these objects. The average(median) magnification values among the first-priority high-z candidates are 6.5 (2.3) in Abell 1835 and 7.9 (3.5) in AC114.

We derived the unlensed L_{1500} luminosity, at 1500 Å in the restframe, for all high-z candidates, using the adopted value $\tilde{z}$ for the redshift and a flux estimate from the photometry in the band closest to this restframe wavelength (SZ, J or H). Deriving the intrinsic properties of $6 \lesssim z \lesssim 10$ galaxies can be challenging due to the significant level of contamination.

After correction by the lensing magnification affecting each object (see Sect. 7.1) the unlensed L_{1500} luminosities were converted into Star Formation Rate (SFR) through the usual calibration from Kennicutt (1998):

$$SFR\ (\mathrm{M_\odot\ yr^{-1}}) = 1.05\ 10^{-40}\ L_{1500}\ (\mathrm{ergs\ s^{-1}\ \AA^{-1}})$$

These physical properties are summarized for each candidate in Table C.2 and C.3. The typical SFR obtained for objects included in the final sample (excluding EROs and anomalous SEDs) is about $\sim 10\ \mathrm{M_\odot\ yr^{-1}}$, with extreme values ranging between a few units and $\sim 20\ \mathrm{M_\odot\ yr^{-1}}$. The conversion of L_{1500} into SFR assumes a constant star formation at equilibrium, and such conditions are not necessarily reached in these objects.

Interestingly, although the selection criteria are only based on near-IR colors irrespective of magnitude, *almost all* the photometric candidates fulfilling our selection criteria are *fainter* than $H = 23.0$ (AB ∼ 24.5). Only three exceptions are found in Abell 1835 among the possible low-z EROs, as described above. After correction for magnification accross these fields, the lack of "bright" sources means that we have not detected young starbursts at $z \sim 6 - 10$ more luminous than typically $L_{1500} = 3 \times 10^{-41}$ ergs s^{-1}, i.e. more massive than typically a few $10^8\ \mathrm{M_\odot}$ (for starbursts younger than 10^6 yr, under standard assumptions for the IMF).

Also, a direct comparison between low-z and high-z SEDs shows that our high-z candidates tend to be very blue in $H - K$. For $z \geq 6$ candidates, $H - K$ colors provide an estimate of the restframe UV slope β, assuming 3σ detection levels in K when the source is not detected in this band, or when the S/N in this band is lower than 3σ, with large uncertainties due to photometric error bars.

The UV slope β usually ranges from -2.5 to -3.5 for the first category dropouts, with two sources (A1835#7 and AC114#2) reaching ~ -3.9 at 1σ, and between -0.7 and -3.0 for the second category dropouts. This systematic trend towards extremely blue colors was also reported by Bouwens et al. (2004b) for their sample of $z \sim 7-8$ candidates.

Although the optical dropouts we found are stretched by the magnification factor μ, they appear as point-like sources in our ground-based images. If we assume a minimum magnification of 0.4 mags for all the field, the physical size of these objects at $z > 7$ is likely to be smaller than 1.7 kpc, in good agreement with size calculations of Kneib et al. (2004) and Bouwens et al. (2004b).

8.2. Observed number counts vs model expectations

The *efficiency* of using lensing clusters as gravitational telescopes to find high-z galaxies can be evaluated with model expectations and simple assumptions.

We first use a simple model to estimate the expected number counts, both in blank fields and lensing clusters, taking into account our photometric selection criteria. We use semi-analytical models for dark-matter halo formation (the Press-Schechter formalism, Press & Schechter 1974). Starburst models presented in Sect. 2 were used to scale the SED, assuming that the fraction of the baryonic mass converted into stars is fixed to $f_* = 0.1$ within the redshift interval $6 \lesssim z \lesssim 11$. We focus on two different "extreme" assumptions for the IMF: a standard Salpeter IMF from 1 to 100 $M_\odot$ and a top-heavy IMF (with stars ranging from 50 to 500 $M_\odot$).

To correct these estimations for the relative *visibility time* of the bursts, which are typically of $t^* = 10^6$ yr timescales from our simulations, we multiply the number density of objects expected at a given redshift z by the *duty-cycle* factor : $t_* \ (1+z)/(t_H(z)-t_H(17))$, where $t_H(z)$ is the age of the Universe at redshift z. This corresponds to the probability for a burst to be visible at redshift z, assuming that all haloes convert a constant fraction of their baryonic mass into stars, at some time between redshifts 17 and z.

Lensing introduces two opposite trends in the observed sample compared to blank fields: 1) gravitational magnification by a factor μ, increasing the number of faint sources and thus the total number of sources, and 2) reduction of the effective surface by the same factor thus leading to a dilution in observed counts. We explicitly compute the expected number counts with these models in clusters by a pixel-to-pixel integration of the magnification maps as a function of redshift, using the lensing models, after masking all the pixels lying in the mask of bright objects described in Sect. 6.2. The expected number counts up to $H \leq 24$ are very similar for the two clusters (less than 10% difference over the redshift interval), and thus we averaged together both results into a unique "strong lensing cluster" prediction. These results hold for intermediate redshift clusters ($z \sim 0.2-0.3$) and should be revised for lensing clusters at higher redshifts and/or a different field of view, although the trends remain the same.

The comparison between expected and observed number counts of galaxies in the field of ISAAC, up to $H \leq 24$, per redshift bin $\Delta z = 1$, in a blank field and in the field of a strong lensing cluster are presented in Fig. 12. Blank field number counts are not corrected for bright-object masking, and thus they correspond to an upper limit. Observed number counts in the two lensing clusters have been corrected for photometric incompleteness (typically a factor of $0.05-0.1$) using the simulations reported in Sect. 5.3, sample incompleteness (by a constant factor $C_{sample} \sim 0.42$ as detailed in Appendix B) and for the expected fraction of false-positive detections, from our estimates given in Table B.1. Results are presented in Fig. 12.

For each redshift bin, we corrected the number counts for both first and second-priority candidates (using $\tilde{z}$ as their redshift estimate), and the results are directly plotted on the model expectations, without any normalization. Observed number counts are upper limits, as our sample is likely contaminated by low-z interlopers.

As shown in Fig. 12, strong lensing fields are a factor of $\sim 5-10$ more efficient than blank fields of the same size in the $z \sim 7-11$ domain, all the other conditions being the same. Observed number counts of candidates at $z \sim 6-8$ are in good agreement with these order of magnitude estimates, in particular with ~10% of the baryonic mass converted into stars at $z \geq 6$. At $z \geq 8$, the observed number counts are more consistent with a top-heavy IMF, with a large cluster-to-cluster variance.

8.3. Lens-corrected number densities of high-z sources

We have used the lensing models to derive the *effective* areas and corresponding volumes surveyed in the different source planes. The aim is to translate the observed number densities of candidates into *effective* number densities easily comparable with blank field studies. We also correct our observed sample of candidates for incompleteness and false-postive detections.

Magnification and dilution effects by the lensing field are carefully taken into account to compute number densities and derived quantities. The average magnification value over a whole ISAAC field is about 2, thus leading to a dilution close to 50% over the whole field. However, a careful modeling is needed to properly take into account the intrinsic incompleteness of the sample as a function of redshift and position on the field. For each candidate in the field, with observed magnitude H_o, we compute the magnification factor $M(\Omega, z)$ as a function of its position and redshift z, as well as the lens-corrected magnitude H_e (referred hereafter as *effective magnitude*), using the lensing models presented in Sect. 7.1. The *effective completeness* $\eta \ (H_e, z)$ gives the ratio between the observed number counts in the lensing field, $N_o(H_e, z)$, and the equivalent

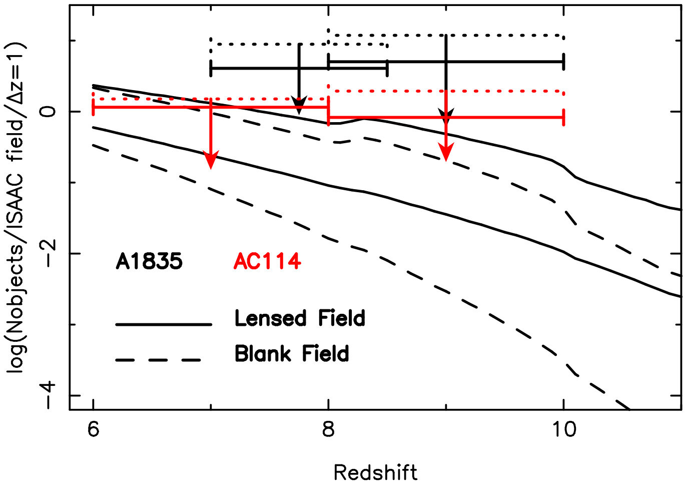

Fig. 12. Comparison between the expected number counts of galaxies in the field of ISAAC, up to $H \leq 24$, per redshift bin $\Delta z = 1$, in a blank field and in the field of a strong lensing cluster (see text for details). Expected counts are obtained with the simple model discussed in Sect. 8.2, for two extreme IMF: a standard Salpeter IMF (lower curves) and a top-heavy IMF (upper curves). The differences between a blank-field (dashed line) and lensing fields (solid lines) are more pronounced at higher redshift. Observed counts are displayed for the two lensing clusters, corrected for incompleteness effects. Solid lines display the results for first-category sources only, whereas dotted lines correspond to first and second-category candidates.

value measured on a blank field of the same observed surface, $N(H_e, z)$, complete up to the magnitude H_e:

$$\eta\ (H_e, z) = \frac{N_o(H_e, z)}{N(H_e, z)}$$

This quantity can be written as a function of the solid angle surveyed on the sky, $\Delta\Omega$,

$$\eta\ (H_e, z) = \frac{\int_{\Delta\Omega} \frac{N(H_e, z)}{M(\Omega, z)} C(H_o) d\Omega}{\int_{\Delta\Omega} N(H_e, z) d\Omega} =$$

$$= \frac{1}{\Delta\Omega} \int_{\Delta\Omega} \frac{C_{sample}\ C(H_e - 2.5\ log_{10} M(\Omega, z))}{M(\Omega, z)} d\Omega$$

where $C(H_o)$ stands for the photometric incompleteness correction for an *observed* H band magnitude H_o (plotted in Fig. 7) and $C_{sample} = 0.42$ is the additional incompleteness factor for the sample, as given in Appendix B.

In practice, we computed the values of η as a function of H_e and redshift using the magnification maps over the field, after masking all the pixels lying in the mask of bright objects described in Sect. 6.2. Figure 13 shows, for each cluster, the location of the candidates in the (z,H_e) plane. Overplotted are different models of high-z starbursts, and completeness levels η. Excluding the 3 brightest EROs in Abell 1835 (which are possibly low-z sources), all our candidates range from H_e=24.0 to 27.2 (AB $\sim$ 25.5 to 28.7). From these diagrams, it appears that our sample of candidates is sensitive to stellar mass scales in the range $10^7 - 10^8$ $M_\odot$, and that our typical correction levels range from 1 to 15% (including both lensing dilution and photometric incompleteness). Candidates with the smallest η factors in these diagrams have the largest weights in the number densities and derived quantities.

8.4. Luminosity Function

A fair estimate of the luminosity function (LF) at 1500 Å can be derived from the intrinsic luminosities of our candidates presented in Sect. 8.1, using the same approach as in the previous section to compute number densities corrected for incompleteness and spurious detections. As discussed in the previous sections, the correction factors applied to this sample are relatively large, thus leading to large error bars in the LF determination. We discuss here two redshift intervals for which we have enough sources for this exercice: $6 \lesssim z \lesssim 10$ and $8 \lesssim z \lesssim 10$. In practice, we derive the number density of objects in the co-volume surveyed, with $\Delta log_{10}(L) = 1$, after correction for the individual η factors. Error bars are estimated as a combination of two independent sources of noise: the 1σ confidence levels for a Poisson distribution and the uncertainty in luminosity introduced by the η factor (typically a factor of 3). The latter is a combination of the photometric error bars, and uncertainties in the incompleteness corrections and lensing modeling. When no object was detected in a luminosity interval, we corrected the Poisson-noise upper limit by the typical effective completeness η for this luminosity. We also corrected our data points for the fraction of false-positive detections expected from Table B.1.

The combined L_{1500} Luminosity Functions for both clusters, with the corresponding error-bars, are given in Fig. 14. Only first and second-priority candidates have been considered, but the difference obtained when using the full sample is within the 1σ error bars.

The observed LFs have been fitted by the STY method (Sandage, Tammann & Yahil 1979), a maximum likelihood fit of data points to the analytical Schechter function $\phi(L)$ (Schechter et al. 1976):

$$\phi(L)dL = \phi^*_{1500} \left(\frac{L}{L^*}\right)^\alpha \exp\left(-\frac{L}{L^*}\right) d\left(\frac{L}{L^*}\right)$$

assuming that this function provides a good representation of the data. Due to a lack of information towards the faint end, a strong degeneracy is expected between L^* and α, which we do not discuss here. To avoid this problem, we assumed a fixed value of $\alpha = 1.6$, corresponding to the Steidel et al. (1999) determination for Lyman Break Galaxies (LBGs) at $z \sim 4$, and leave the other parameters free. The typical values found for L^* are $10^{41.5}$ ergs s^{-1} s^{-1} Å $^{-1}$, and these results are not affected by the way we binned the data points. The STY fits to the data presented in Fig. 14.

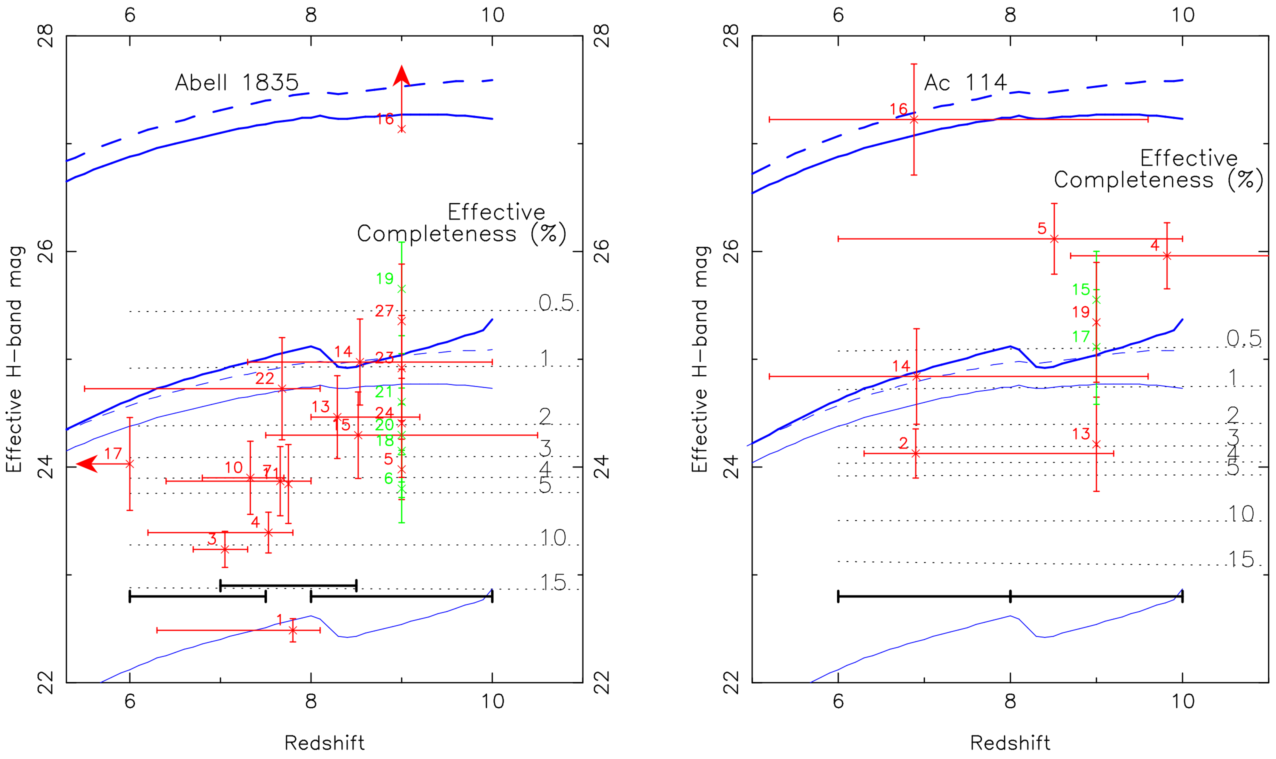

Fig. 13. Effective magnitudes H_e, corrected for lensing, as a function of z for the two lensing clusters. Values of effective completeness $\eta(H_e, z)$ with respect to a blank field (for number counts complete up to H_e) are overplotted as dotted lines for the 0.5 to 40% levels (see text for details). First and second-category (red) and third-category (green) candidates are positioned at their adopted redshift $\tilde{z}$, with errors bars in z corresponding to $[z1-z2]$ range (see text for details). Redshift intervals considered for third-category candidates are given at the bottom of the figure. Photometric errors in H_e coincide with photometric errors observed in H. Solid lines display the predicted magnitudes versus redshift for 4 different starbursts models used in Sect. 2, with a stellar masses scaling to 10^7 M$_\odot$ (thick line) and 10^8 M$_\odot$ (thin line). From top to bottom, these models correspond to single bursts with Salpeter IMF and stellar masses ranging from (1) 1 and 100 M$_\odot$, and (2) 50 and 500 M$_\odot$. For comparison, the dashed line corresponds to a constant star-forming model with age 10^8 yr.

Without the blind correction for false-positive detections, the data points increase by ∼0.4-0.6 dex, which is a relatively small effect compared to the error bars.

For comparison, we overplot in Fig. 14 the LF fit found by Steidel et al. for LBGs at $z \sim 3$, after correction for differences in the respective cosmological parameters. It is shown as a thick dashed line in Fig. 14 *without any renormalization* to fit the data points. This LF for LBGs at $z \sim 3$ seems to be slightly higher (by ~ 0.5 dex) than the LF for our candidates, but compatible within the 1σ error bars. Our results are also fully compatible with the LF derived by Bouwens et al. (2005) (presented as a dotted line in Fig. 14) for their sample of $z \sim 6$ candidates in the UDF, UDF-Ps and GOODS fields in the low-luminosity regime, i.e. for $L_{1500} \lesssim 0.3 L^*_{z=3}$, but we do not see the turnover observed by these authors towards the bright end relative to the $z \sim 3$ LF.

We also display in Fig. 14 the LF derived from the simple models presented in Sect. 8.2, in the redshift intervals $6 \lesssim z \lesssim 10$ (red lines) and $8 \lesssim z \lesssim 10$ (black lines), for the standard Salpeter IMF (thin dashed lines) and the top-heavy IMF (thin solid lines). A better overall fit to data points is obtained with the top-heavy IMF.

Considering only first-priority or first+second priority candidates does not change the results substantially. Also, including or removing the brightest EROs in Abell 1835 does not change these conclusions.

8.5. Cosmic Star Formation Rate at $z > 6$

We use the individual properties computed in Sect. 8.1 to derive the Cosmic SFR value for each redshift bin considered in our previous analysis. The large correction factors applied to this sample, which dominate the error bars on LF measurements, make the determination of SFR densities challenging. We use different approaches here to derive an estimate for this important quantity. On the other hand, since these objects are only photometric candidates, the obtained values are to be considered as upper limits. However, all values derived here neglect possible extinction corrections.

The first estimate is obtained in a very simple way. We compute the total SFR in a redshift bin by summing

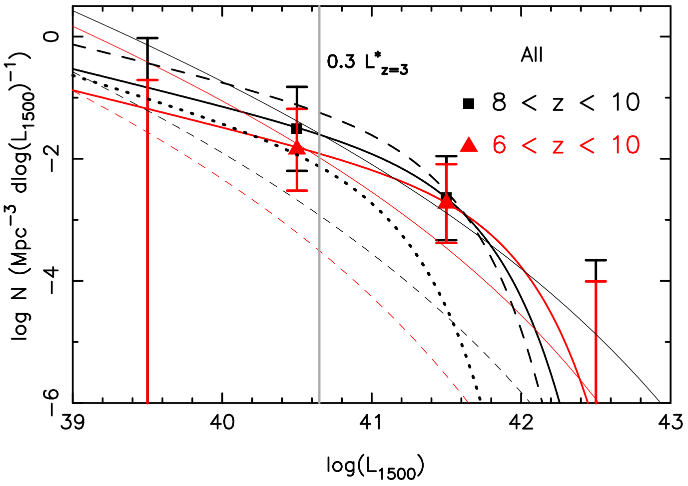

Fig. 14. Combined L_{1500} LFs for the two fields, for two redshift intervals: $6 \lesssim z \lesssim 10$ (red) and $8 \lesssim z \lesssim 10$ (black). Data points are corrected for spurious sources, and error bars combine Poisson noise statistics and uncertainty in the effective completeness. Note the large correction factors applied to this sample, which translate into large error bars. The STY fits to the LF data are represented by thick solid lines. For comparison, the LF fit by Steidel et al. for LBGs at $z \sim 3$ is also overplotted (thick dashed line), as well as the $z \sim 6$ fit from Bouwens et al. (2005) (thick dotted line), *without any additional renormalization to fit the data*. Also the L_{1500} LF derived from the simple models presented in Sect. 8.2 is shown, in the redshift intervals $6 \lesssim z \lesssim 10$ (red thin lines) and $8 \lesssim z \lesssim 10$ (black thin lines), for the classical salpeter IMF (dashed lines) and the top-heavy IMF (solid lines). The cosmic SFR value has been derived by integrating this LF down to $0.3L^*_{z=3}$ (shown as a vertical grey line). See text for more details.

all individual contributions to the SFR within this bin, after correcting each object by its η value and its expected probability of being a false-positive detection (Table B.1). We divide this result by the total covolume surveyed in this redshift bin accross the ISAAC field area, assuming a blank field (because magnification/dilution effects are already included in the η factor). This corresponds to $2.9\ 10^4$ Mpc^3 for $z \in [6-7.5]$, $2.6\ 10^4$ Mpc^3 for $z \in [7-8.5]$, $3.8\ 10^4$ Mpc^3 for $z \in [6-8]$, $3.1\ 10^4$ Mpc^3 for $z \in [8-10]$, for the size of an ISAAC field. The resulting SFR densities $\rho_\star$ obtained are relatively high, even when the sample is restricted to first and second-category candidates: $\rho_\star = 3.31\ 10^{-3}$ M$_\odot$ yr^{-1} Mpc^{-3} for $z \in [6-7.5]$, $2.46\ 10^{-2}$ M$_\odot$ yr^{-1} Mpc^{-3} for $z \in [7-8.5]$, and $1.20\ 10^{-1}$ for $z \in [8-10]$.

Another estimate of the cosmic SFR, allowing us to compare results to previous findings, can be obtained by integrating the Luminosity Function fit found in Sect. 8.4 down to $0.3\ L^*_{z=3}$, the same limit used by Bouwens et al. (2004b). In this case, we use the same redshift bins defined in Sect. 8.4, and we obtain a somewhat lower value of the SFR for z in [6-10] if we consider the first and second category candidates. Considering only the first category candidates, these values are lower by a factor ~ 3, as can be seen from Table 3, summarising our different cosmic SFR density estimates.

The final results are shown in Fig. 15, applying the correction for false-positive detections, for comparison with the cosmic SFR obtained in other surveys carried out on blank fields, without applying any extinction correction. Our error bars were computed using Poisson noise statistics in the number of objects within each redshift bin. The numerical values of the cosmic SFR are also summarized in Table 3.

When considering only the first-category candidates (i.e with a 1σ error $\Delta m_H < 0.4$), our results in the $z \sim 6-10$ domain are compatible with previous findings. However, our estimate of the comoving SFR density at $z \sim 8-10$ seems to be larger than all values derived at $z \sim 4-6$, although compatible within the error-bars. Taken at face value, our findings seem to be in good agreement with some theoretical cosmic SFR density models previously published; e.g. with the model of Barkana & Loeb (2001, their Fig. 29) for a reionization redshift between 6 and 8, recent hydrodynamical models of Nagamine et al. (2005), and with the self-consistent reionization models of Choudhury & Ferrara (2005).

However, compared to recent studies in the Hubble UDF at similar redshifts (Bouwens et al. 2004b, 2005a) our SFR density, or upper limits thereof, is larger by roughly 1 dex. This difference is related to the bright end of the LF, i.e. $L_{1500} \gtrsim 0.3L^*_{z=3}$. In all cases the sources are photometric candidates therefore providing upper limits to the actual UV flux densities. The effective fields surveyed are small in all cases, thus leading to a strong field-to-field variation of $\sim 20-30\%$ in the number of sources. Cluster-to-cluster variations already discussed in Sect. 7.6 are clearly seen in our sample, although lensing and photometric considerations could account for most of them. Recent spectroscopic results obtained by Le Fèvre et al. (2005) on the VVDS, for an I-band flux-limited sample of galaxies up to $z \sim 5$, indicate that the Universe contains more star-forming galaxies towards the bright end of the LF than previously reported using color-color selection techniques, suggesting an active star formation activity in the redshift domain covered by the present survey.

There are several ways to reconcile our SFR measurements with Bouwens et al.'s values, in addition to field-to-field variance. Residual contamination by false sources combined with lensing effects are able to affect our results in different ways.

On the one hand, residual spurious sources constitute a potential source of contamination if the adopted corrections are underestimated. The extremely blue H-K colors obtained for the stacked images argue for a significant residual contamination for the faint third category dropouts, as discussed in detail in Appendix C. For this reason, third category dropouts were not used to derive LFs and SFR densities. The blind corrections applied to the first and second-category samples to obtain the above results are in good agreement with the contamination levels derived from the stacked images and the UV slope.

On the other hand, *observed* number counts could be affected by residual positive magnification bias, producing a systematic trend compared to blank fields. This trend is indeed expected under simple considerations, as shown in Sect. 8.2 and Fig. 12. A positive magnification bias is expected when the slope of number counts (with the approximation $\alpha = -d(log\ n)/d(log\ L)$) is $\alpha \lesssim -1$ in the magnitude and redshift domains considered, i.e. $N_{lensed}(>L) = N(>L) \times \mu^{\alpha-1}$ (see e.g. Broadhurst et al. 1995). This is indeed the case within our H band limited sample, according to the simple assumptions given in Sect. 8.2, and the shape of the observed LF. We have directly accounted for magnification biases using the lensing models. However, an additional magnification bias could remain in our sample due to a systematic trend: up to a given limiting magnitude, we tend to detect the sources with the largest magnification factors, instead of (or in addition to) the intrinsically brighter sources, as it happens in blank fields. This systematic trend could slightly modify the slope of the LF derived for high-z sources. It is difficult to correct for without a complete mock simulation, assuming a shape for the LF of background sources, and then statistically correcting for this additional bias. Given the error bars obtained for the LF in Sect. 8.4, this residual magnification bias should be a second order correction for high-z sources. However, the same trend could exist for very faint intermediate-redshift interlopers, such as the extremely-faint source A1835#35 (Richard et al. 2003). This effect is presently uncorrected in our sample for obvious reasons, but it could be responsible for part of the discrepancy, because intermediate-redshift interlopers should mainly affect the bright end of the LF.

The standard calibration used to convert the L_{1500} luminosity into SFR, which assumes a standard Salpeter IMF under equilibrium conditions (i.e. constant SF over timescales $\gtrsim 10^{8-9}$ yr), is not necessarily appropriate for objects at such early epochs.

Table 3. Summary of results obtained for the comoving Star Formation Rate density (in $M_\odot$ yr^{-1} Mpc^{-3}) by integrating the Luminosity Function down to 0.3 $L^*_{z=3}$ in different redshift ranges, also presented in Fig. 15, correcting for lensing, incompleteness effects and expected fraction of spurious sources.

Assumption	SFR density
$[6-10]$ First-category	2.7 10^{-2}
$[6-10]$ First and second-category	7.4 10^{-2}
$[8-10]$ First-category	3.5 10^{-2}
$[8-10]$ First and second-category	1.1 10^{-1}

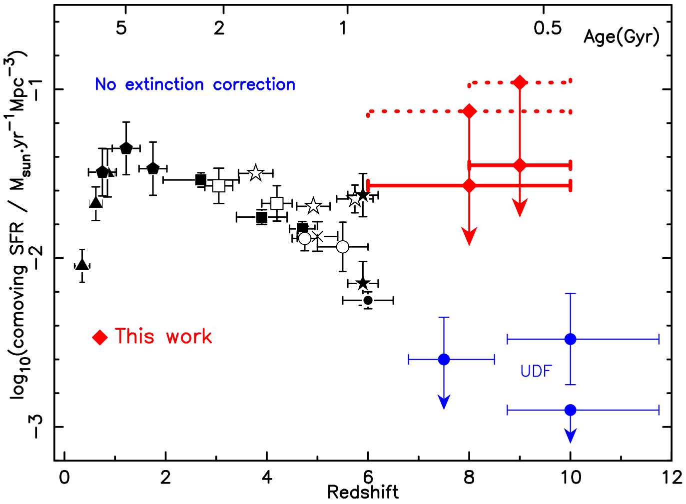

Fig. 15. Evolution of the comoving Star Formation Rate density as a function of redshift. Different approaches are used to derive an order of magnitude estimate for this quantity, reported in Table 3. Results from other surveys, uncorrected for extinction, are compared to our upper limits taken at face value. Data are compiled from the CFRS (Lilly et al. 1995, filled triangles), Connolly et al. 1997 (filled pentagons), LBG work from Steidel et al. 1999 (open squares), Fontana et al. 2003 (open circles), Iwata et al. 2003 (cross), Bouwens et al. 2003a (filled squares), GOODS (Giavalisco et al. 2004, open stars), different ACS estimates from Bouwens et al. 2003b (filled stars) and Bouwens et al. 2005b (filled circle). We also report the value derived by Bouwens et al. (2004b) and Bouwens et al. (2005a) in the Ultra-Deep Field ("UDF" labels). Our results (filled red diamonds) are presented for both clusters in the redshift ranges $[6-10]$ and $[8-10]$: these values are obtained by integrating the Luminosity Function fit down to $L_{1500} = 0.3\ L^*_{z=3}$. Solid lines refer to the first-category candidates only ($\Delta m_H < 0.4$), whereas dotted lines correspond to first and second-category sources.

8.6. Spectroscopic follow-up

We have started the spectroscopic follow-up of our sample of high-z candidates with ISAAC/VLT. This survey is presently ongoing, and the final conclusions will be presented in a further paper. Results on these observing runs have been (partly) published in Richard et al. (2003) and Pelló et al. (2004a), as well as a first preliminary summary in Pelló et al. (2004b).

To search for faint emission lines, we have systematically explored the 0.9-1.40 μm domain (SZ and J bands of ISAAC), where Lyα should be located for objects within the $7 < z < 10.5$ redshift interval. We intended to detect emission lines with intensities ranging between 10^{-17} and a few 10^{-18} ergs s^{-1} cm^{-2} Å^{-1}, with a spectral resolution for the sky lines of $R = 3100$ corresponding to the instrumental 1$''$ slit width. The fraction of spectral band lost due to strong OH sky emission lines is of the order of 30%. Slit configurations were set to optimize the acquisition of a maximum number of targets per night, with priority given to first-category dropouts. Secondary targets were only observed when aligned with first priority targets.

Up to now, our spectroscopic survey with ISAAC has targeted 2 priority candidates in AC114, and 7 in Abell 1835 (4 "first priority" targets and 3 secondary ones). From this sample of 9 targets, 2/3 of the objects observed display emission lines. 5 sources have clear emission lines detected, and another one is still to be confirmed. The distribution between first and second priority targets for spectroscopy does not fully coincide with the present classification in Tables C.2 and C.3, because it was based on an earlier version of the image reduction and analysis. For instance, z and SZ images were not available for Abell 1835 at this epoch. In summary, from 6 first priority spectroscopic targets observed in the two clusters, we have clearly confirmed one candidate (A1835#8, originally named A1835-1916, see Sect. 7.4), which is found to be a puzzling source; two $z \geq 7$ candidates show emission lines still to be reconfirmed; one candidate is found to be a low-z contamination, and two of them do not show emission lines. From the 2/3 secondary targets displaying emission lines, one is a possible $z \geq 7$ source to be confirmed, whereas the other one is a faint low-z galaxy (A1835#35, $z = 1.67$). According to these preliminary numbers, the efficiency of our survey could range between ~ 30 and 50%, with interesting low-z by-products such as A1835#35 (Richard et al. 2003). A large majority of our high-z candidates still need to be confirmed, either by a redetection of a faint emission line, or by the non-detection of other lines expected at low-z.

9. Summary and conclusions

We have obtained deep JHK near-IR photometry of two well-known lensing clusters, A1835 and AC114, plus z and SZ imaging of A1835 with FORS and ISAAC at the VLT. Our photometric depth reached $SZ \sim 25.6$, $J \sim 24.4$, $H \sim 23.5$ and $K_s \sim 23.3$ (Vega system), in addition to a minimum magnification factor of 1 magnitude over half of the ISAAC field of view. These images, combined with existing data in various optical bands including HST images, have been used to select galaxy candidates at very high redshift ($z \sim 6-10$). The candidates have been selected with the dropout technique and two-color selection criteria appropriate for high-z galaxies.

From our H band selected sample we have identified 18 (8) "first and second-category" optical dropouts in A1835 (AC114) up to $H_{\rm Vega} \sim 23.9$ (AB ~ 25.3, uncorrected for lensing). Second category is defined here as objects detected in ≥ 2 near-IR bands, the best-detected sources being defined as first priority. Among them, 8(5) exhibit homogeneous SEDs compatible with star-forming galaxies at $z \gtrsim 7$, and 5(1) are more likely intermediate-redshift EROs. In both fields we have also identified a few additional dropouts detected only in the H band ("third category" objects), which satisfy our photometric selection criteria. We have estimated the fraction of spurious sources expected in the different filter combinations, and corrected all the relevant derived quantities for this effect.

Typically our candidates are magnified by a factor of 1.5 (~ 0.44 mags) to 10 (2.5 mags), with average (median) values of the order of $6.5-7.9$ ($2.3-3.5$) for the two clusters. All high-z candidates turn out to be fainter than $H_{\rm Vega} \sim 23$, with typical effective (i.e. lensing corrected) magnitudes $H_{\rm Vega} \sim 24-25$ ($H_{\rm AB} \sim 25.4-26.4$) and fainter in some cases. Assuming standard SFR(UV) conversion factors, which may however be questionable for galaxies of such presumably young age, the SFR is found to be between few units and ~ 20 M$_\odot$ yr^{-1}. Their UV restframe spectrum, measured by the $H-K$ color, seems to be very blue – a trend also reported for other high-z galaxy samples (e.g. Papovich et al. 2004, Bouwens et al. 2004b).

Taking into account the gravitational lensing effects, sample incompleteness and expected spurious detections, a first attempt was made to constrain the density of star-forming galaxies present at $z \sim 6-10$ based on lensing data. Integrated quantities, such as LFs and SFR densities, are affected by non-negligible uncertainties due to the large correction factors applied to this sample. The LF measured for LBGs at $z \simeq 3$ seems to be slightly higher (by ~ 0.5 dex) but still consistent with the LF derived for our sample. The turnover observed by Bouwens et al. (2005) towards the bright end relative to the $z \sim 3$ LF is not observed in this sample.

We have also estimated an upper limit for the cosmic SFR density from these data. Our values in the $z \sim 6-10$ domain are higher than the estimates obtained in the NICMOS UDF, even when the most conservative assumptions and corrections are applied to the data. This difference is related to the bright end of the UV LF for our candidates, i.e. $L_{1500} \gtrsim 0.3 L^*_{z=3}$. This systematic trend with respect to blank fields could be due to to field-to-field variance, a positive magnification bias from intermediate-redshift EROs, and/or residual contamination by spurious sources. Given the error bars, residual magnification bias should be negligible for high-z sources, but a population of faint intermediate-redshift interlopers affected by positive magnification bias cannot be excluded. At least one of such intermediate sources was spectroscopically identified in the field of A1835 (Richard et al. 2003).

According to our simulations, in agreement with the first photometric results presented in this paper, the use of lensing clusters as gravitational telescopes seems to significantly improve the survey efficiency of $z \gtrsim 6$ galaxies compared to blank fields.

Given the uncertainties involved in the candidate-selection process, and the faint fluxes observed for our photometric candidates, the present results are to be considered as a first attempt to constraint the population of $6 \lesssim z \lesssim 10$ star-forming galaxies using lensing clusters. The present results and conclusions have to be confirmed and improved. Spectroscopic follow-ups are underway to determine the efficiency of our selection technique, and the contamination level by intermediate-redshift interlopers. Additional deep photometry in various bands are being secured with HST, IRAC/Spitzer, and from the ground to improve the SEDs characterization of the high-z candidates. Increasing the number of lensing fields with ultradeep near-IR photometry is essential to obtain more accurate constraints on the abundance and physical properties of $z \gtrsim 7$ starburst galaxies.

Acknowledgements. We are grateful to T. Contini, G.P. Smith, E. Egami, F. Lamareille, A. Hempel, C. Donzelli for useful comments and discussions, and to the anonymous referee for his/her helpful and constructive comments. We thank the ESO Director General for a generous allocation of Director's Discretionary Time for ISAAC spectroscopy (DDT 271.A-5013 and 272.A-5049). JR and JPK are grateful to Caltech, and in particular to R.S. Ellis, for their support. This paper is also based on observations collected at the European Space Observatory, Chile (069.A-0508,070.A-0355,073.A-0471), the NASA/ESA Hubble Space Telescope operated by the Association of Universities for Research in Astronomy, Inc., and the Canada-France-Hawaii Telescope operated by the National Research Council of Canada, the French Centre National de la Recherche Scientifique (CNRS) and the University of Hawaii. Part of this work was supported by the French *Centre National de la Recherche Scientifique*, the French *Programme National de Cosmologie* (PNC) and *Programme National de Galaxies* (PNG), by the *International Space Science Institute* (ISSI), as well as by the Swiss National Science Foundation.

References

Barger, A.J., Aragón-Salamanca, A., Ellis, R.S., Couch, W.J., Smail, I., Sharples R.M., 1996, MNRAS, 279, 1.

Barkana, R. & Loeb, A. , 2001, Physics Reports, 349, 125

Barton, E. J., Davé, R., Smith, J. T., Papovich, C., Hernquist, L., & Springel, V. 2004, ApJ, 604, L1

Bertin, E., Arnouts, S., 1996, A & AS, 117,393.

Bolzonella, M., Miralles, J.M., Pelló, R., 2000, A & A, 363, 476.

Bouwens R., Broadhurst T., Illingworth G., 2003a, ApJ, 593, 640.

Bouwens R., et al. , 2003b, ApJ, 595, 589.

Bouwens, R. J., Illingworth, G. D., Blakeslee, J. P., Broadhurst, T. J., & Franx, M. 2004a, ApJ, 611, L1.

Bouwens R. J., Thompson R. I., Illingworth G. D., Franx M., van Dokkum P., Fan X., Dickinson M. E., Eisenstein D. J., Rieke M. J., 2004b, ApJ, 616, L79

Bouwens, R. J., Illingworth, G. D., Thompson, R. I., Franx, M., 2005a, ApJ, 624, L5.

Bouwens, R. J., Illingworth, G. D., Blakeslee, J. P., Franx, M., 2005b, ApJ, in press.

Bremer, M. N., Jensen, J. B., Lehnert, M. D., Schreiber, N. M. F., & Douglas, L. 2004, ApJ, 615, L1

Broadhurst, T. J., Taylor, A. N., & Peacock, J. A. 1995, ApJ, 438, 49

Bromm, V. , Kudritzki, R.P., Loeb, A., 2001, ApJ, 552, 464.

Bruzual, G., Charlot, S. 1993, ApJ, 405, 538.

Bunker, A.J., Stanway, E.R., Ellis, R.S., McMahon, R.G., McCarthy, P.J., 2003, MNRAS, 342, L47 .

Calzetti, D., Armus, L., Bohlin, R.C., Kinney, A.L., Koornneef J., Storchi-Bergmann T. 2000, ApJ, 533, 682.

Campusano, L.E., Pelló, R., Kneib, J.-P., Le Borgne, J.-F., Fort, B., Ellis, R., Mellier, Y., Smail, I., 2001, A & A, 378, 394.

Choudhury, T.R., Ferrara, A., 2005, MNRAS, 361, 577.

Coleman, D.G., Wu, C.C., Weedman, D.W. 1980, ApJS, 43, 393.

Connolly, A. J., Szalay, A. S., Dickinson, M., Subbarao, M. U., & Brunner, R. J. 1997, ApJ, 486, L11.

Couch, W.J., Balogh, M. Bower, R.G., Smail, I., Glazebrook, K., Taylor, M., 2001, ApJ, 549, 820.

Cuby, J.G., et al., 2000, Proc. SPIE Vol. 4008, p. 1036-1R047 Optical and IR Telescope Instrumentation and Detectors, Masanori Iye; Alan F. Moorwood; Eds.

Cuby, J.G., Lidman, C., Moutou, C., Johnson, R., Doublier, V., 2002, ISAAC User Manual, v. 1.10.1

Cuby, et al. 2003, A&A, 405, L19.

Czoske, O., Kneib, J.-P., Bardeau, S., 2002, in "Matter and Energy in Clusters of Galaxies"; ASP Conf. Series, eds. S. Bowyer & C.-Y. Hwang, [astro-ph/0211517]

Daddi, E., Cimatti, A., Pozzetti, L., Hoekstra, H., Rottgering, H.J.A., Renzini, A., Zamorani, G., Mannucci, F., 2000, A & A, 361, 535.

Ebeling, H., Edge, A. C., Bohringer, H., Allen, S.W., Crawford, C.S., Fabian, A.C., Voges, W., & Huchra, J. P., 1998, MNRAS, 281, 799.

Ellis, R., Santos, M. R., Kneib, J.-P., Kuijken, K., 2001, ApJ, 560, L119.

Fan, X., et al. 2002, AJ, 123, 1247.

Fontana A., Poli F., Menci N., Nonino M., Giallongo E., Cristiani S., D'Odorico S., 2003, ApJ, 587, 544.

Franx, M., Illingworth, G. D., Kelson, D. D., van Dokkum, P. G., & Tran, K., 1997, ApJ, 486, L75.

Frayer, D. T., Reddy, N. A., Armus, L., Blain, A. W., Scoville, N. Z., & Smail, I. 2004, AJ, 127, 728

Gal-Yam, A., Maoz, D., & Sharon, K. 2002, MNRAS, 332, 37

Giavalisco M., et al., 2004, ApJ, 600, L103.

Haiman, Z., Loeb, A. 1999, ApJ, 519, 479.

Heckman, T. M., Robert, C., Leitherer, C., Garnett, D. R., & van der Rydt, F. 1998, ApJ, 503, 646

Hu, E. M., Cowie, L. L., McMahon, R. G., Capak, P., Iwamuro, F., Kneib, J.-P., Maihara, T., & Motohara, K. 2002, ApJ, 568, L75.

Ivison, R. J., Smail, I., Barger, A. J., Kneib, J.-P., Blain, A. W., Owen, F. N., Kerr, T. H., & Cowie, L. L. 2000, MNRAS, 315, 209

Iwata I., Ohta K., Tamura N., Ando M., Wada S., Watanabe C., Akiyama M., Aoki K., 2003, PASJ, 55, 415.

Izotov, Y.I., Chaffee, F.H., Schaerer, D. 2001, A& A, 378, L45.

Kennicutt, R. C. 1998, ARA&A, 36, 189

Kinney, A.L., Calzetti, D., Bohlin, R.C., McQuade, K., Storchi-Bergmann, T., Schmitt, H.R. 1996, ApJ 467, 38.

Kneib, J.-P., Ellis, R.S., Santos, M.R., Richard, J., 2004, ApJ, 607, 697.

Kodaira, K., et al. 2003, PASPJ 55, L17.

Labbé, I., Franx, M., Rudnick, G., Schreiber, N.M.F., Rix, H.W., Moorwood, A., Van Dokkum, P.G., Van der Werf, P., Röttgering, H., Van Starkenburg, L., Van de Wel, A., Kuijken, K., Daddi, E., 2003, AJ, 125, 1107.

Lemoine-Busserolle, M., Contini, T., Pelló, R., Le Borgne, J.-F., Kneib, J.-P., Lidman, C., 2002, A & A, 397, 839.

Le Fèvre, O., Paltani, S. et al. 2005, Nature, 437, 519.

Lehnert, M. D., Förster Schreiber, N. M., & Bremer, M. N. 2005, ApJ, 624, 80

Lilly, S. J., Le Fevre, O., Hammer, F., & Crampton, D. 1996, ApJ 460, L1.
Loeb, A. & Rybicki, G.B. 1999 ApJ, 524, 527.
Loeb, A. & Barkana, R., 2001, ARA& A, 39, 19.
Madau, P. 1995, ApJ, 441, 18.
Marri & Ferrara 1998, ApJ,509, 43.
Marri, S., Ferrara, A., & Pozzetti, L. 2000, MNRAS, 317, 265
Mobasher, B., Dickinson, M., Ferguson, H.C. et al., 2005, ApJ, 635, 832
Monet, D. G., 1998, American Astronomical Society Meeting, 193, 112.003
Moorwood, A.F., 1997, Proc. SPIE Vol. 2871, p. 1146-1151, Optical Telescopes of Today and Tomorrow, Arne L. Ardeberg; Ed.
Natarajan, P., Kneib, J.-P., Smail, I., Ellis, R.S., 1998, ApJ, 499, 600.
Nagamine, K., et al., 2005, in " First Light and Reionization: Theoretical Study and Experimental Detection of the First Luminous Sources in the Universe", Eds. A. Cooray, E. Barton, New Astronomy Reviews, in press

Noll, S., et al. 2004, A&A, 418, 885
Papovich, C., Dickinson, M., Ferguson, H. C. et al., ApJ, 2004, 600, 111L
Pelló, R., Schaerer, D. 2002, "Science with the GTC" conference, astroph/0203203.
Pelló, R., Schaerer, D., Richard, J., Le Borgne, J.-F., Kneib, J.-P., 2004a, A & A, 416, L35.
Pelló, R., Schaerer, D., Richard, J., Le Borgne, J.-F., Kneib, J.-P., 2004b, Proceedings of IAU Symposium No. 225: The Impact of Gravitational Lensing on Cosmology, Y. Mellier and G. Meylan, Eds., [astro-ph/0410132]
Persson, S.E., Murphy, D.C., Krzeminski, W., Roth, M., Rieke, M.J., AJ, 116, 2475.
Pickles A. J., 1998, PASP, 110, 863
Press, W. H. & Schechter, P., 1974, ApJ, 187, 425.
Richard, J., Schaerer, D., Pelló, R., Le Borgne, J.-F., Kneib, J.-P., 2003, A & A, 412, L57.
Sandage, A., Tammann, G. A. & Yahil, A. 1979, ApJ 232, 352
Schaerer, D. 2002, A & A, 382, 28.
Schaerer, D. 2003, A & A, 397, 527.
Schaerer, D. & Pelló R., 2001, in "Scientific Drivers for ESO future VLT/VLTI Instrumentation", J. Bergeron and G. Monnet, Eds., Springer Verlag, p.48, astroph/0107274.
Schaerer, D., & Pelló, R. 2005, MNRAS, 362, 1054
Schechter, P. 1976, ApJ, 203, 297
Smail, I., Ellis, R.S., Fitchett, M.J., Norgaard-Nielsen, H.U., Hansen, L., Jorgensen, H.E., 1991, MNRAS, 252, 19.
Smail, I., Couch, W.J., Ellis, R.S., Sharples, R.M., 1995, ApJ, 440, 501.
Smail, I., Ivison, R.J., Kneib, J.-P., et al., 1999, MNRAS, 308, 1061.
Smail, I., Ivison, R. J., Blain, A. W., & Kneib, J.-P. 2002, MNRAS, 331, 495
Smith, G. P., Kneib, J.-P., Smail, I., Mazzotta, P., Ebeling, H., & Czoske, O. 2005, MNRAS, 359, 417
Smith, G. P., Sand, D. J., Egami, E., Stern, D., & Eisenhardt, P. R. 2006, ApJ, 636, 575
Shapley, A.E., et al., 2003, ApJ, 562, 95.
Spergel, D. et al. 2006, ApJ submitted [astro-ph/0603449]
Steidel, C. C., Pettini, M., & Hamilton, D. 1995, AJ, 110, 2519
Steidel, C. C., Adelberger, K. L., Giavalisco, M., Dickinson, M., & Pettini, M. 1999, ApJ, 519, 1.
Steidel, C. et al., 2003, ApJ, 592, 728.
Spinrad, H., 2003, "Astrophysics Update" in press, [astro-ph/0308411]
Stanway, E. R., Bunker, A. J., McMahon, R. G., et al. 2004, ApJ, 607, 704
Stern, D. et al. 2004, ApJ, 612, 690.
Trujillo, C. A., Jewitt, D. C., & Luu, J. X. 2001, AJ, 122, 457
Thompson, R.I., Illingworth, G., Bouwens, R., et al., 2005, AJ accepted, [astro-ph/0503504]
Tumlinson, J., Shull, M., 2000, ApJ, 528, L65

Online Material

Appendix A: Further improvements in the data reduction

The following steps were introduced in addition to the standard scheme to improve the data reduction:

- Object masks created by XDIMSUM were not well-suited for our fields centered on lensing clusters, because they did not correctly take the bright extended haloes in the cluster core into account. We improved the sky-subtraction in these regions by applying a simple threshold above the sky background in our images to create the object masks. This procedure greatly reduced the contamination close to the bright objects.
- About 35 % of the images taken with the Hawaii-Rockwell array suffered from bias residuals, that appear more pronounced at the bottom and middle region of the detector. Before combining the individual sky-subtracted frames, we removed these residuals by subtracting from each line its median, with a rejection of pixels flagged in the object mask.
- In the case of AC114 cluster, about 20% of the individual H band frames presented strong low-frequency background variations, due to imperfect sky-subtraction and possible contamination due to the proximity of the moon. We corrected part of these residuals using a bidimensional fit of the large-scale background for each frame, after rejection of all pixels flagged in our object mask.
- Before combining the frames into a final stack, we applied weight values accounting for slight variations in quality during observations, in such a way that the best-quality images will have the highest weight. Weighting was optimized in order to improve the detectability of faint point-like sources ; we computed individual weights using the following relation :

  $$weight \propto (ZP \times var \times s^2)^{-1}$$

  where we computed the individual zero-point ZP and seeing s from the magnitudes and FWHM of the 5 brightest unsaturated stars located in our field. The local sky pixel-to-pixel variance var was derived through background statistics inside a small region free of objects.
- To check for the final accuracy of our absolute photometric calibration, we compared the theoretical and observed colors of several cluster elliptical galaxies for which we had available spectroscopy, after having reduced the images as described below, and seeing-matched them to the worst value. The empirical SED template compiled by Coleman, Wu and Weedman (1980) was used to derive the expected colors for elliptical galaxies at the cluster redshifts. In the single case of the J band image in Abell 1835, we corrected a 0.1 mag offset in the zero-point. We also checked that the optical to near-IR colors of the brightest elliptical galaxies were consistent with the theoretical expectations. We found that our final absolute photometry is accurate to about 0.05 mag throughout the wavelength domain.

Appendix B: Sample completeness and false-positive detections

In addition to the purely photometric completeness effect in the detection of near-infrared sources, another incompleteness factor comes directly from our non-detection criterion in the optical bands. We statistically expect, by integrating a normal distribution function above this level, to measure a 1σ flux for 16 % of all dropouts in each optical band, which we did not include in our current selection technique. Because there are 5 such non-detection filters for each cluster, this gives a statistical completeness factor of $C_{sample} = (1-0.16)^5 \sim 0.42$, which is unrelated to the observed NIR magnitude of the objects. We applied this additionnal correction to the final sample of optical dropouts.

Our detection scheme was optimized to identify faint sources which are only detected on the near-IR bands, i.e. a subsample of the images. To evaluate the fraction of spurious detections expected in our photometric catalogs, we constructed a special *noise image* for each cluster and each near-infrared band, where all astronomical sources were removed while keeping the same noise properties: we subtracted by pairs sequential images obtained with similar seeing conditions, and then coadded them using the same procedure described above. The result is an image with the same noise properties compared to the final stacks, affected only by small residuals at the location of the brightest sources. We used *SExtractor* to detect objects inside these noise images, with the "double-image" mode and the same detection parameters as for astronomical sources. After masking the regions around the brightest objects and galaxy haloes to prevent any detection of source residuals (as for the astronomical images), the number of objects detected in these noise images was compared with the number of high-z candidates *blindly* selected as optical-dropouts within the same region on the astronomical images, for different ranges of magnitude and categories of optical dropouts as defined in Sect. 6.2. H-band magnitude bins have been defined to include a similar number of spurious sources in each bin. A source was conservatively included as positive (spurious) detection in this table when Sextractor in the double-image mode was able to measure a magnitude for this source above the same detection level as defined for our candidates in Sect. 6.2. Results are summarized in Table B.1 for each cluster.

The fraction of false objects obtained with this procedure is overestimated compared to real catalogs, since no attempt was made to manually correct for obvious spurious detections, whereas all the dropout candidates included in the final catalogs were visually inspected by at least two different persons. Their false-detection probability is therefore reduced compared to Table B.1.

Appendix C: Additional tests on the reliability of optical dropouts

In addition to the simulations presented in Sect. 5.3 on the completeness and spurious detections expected on the reference H band image and on the other near-IR images, we have performed additional tests on the reliability of optical-dropouts identified on the near-IR images.

C.1. Pseudo-χ^2 images

Detection pseudo-χ^2 images were created from individual J, H and Ks band images in the following way : each image was normalized by the noise 1σ image, weighted by the square root of the corresponding exposure-time maps, and then all images were registered and averaged together. We applied the same

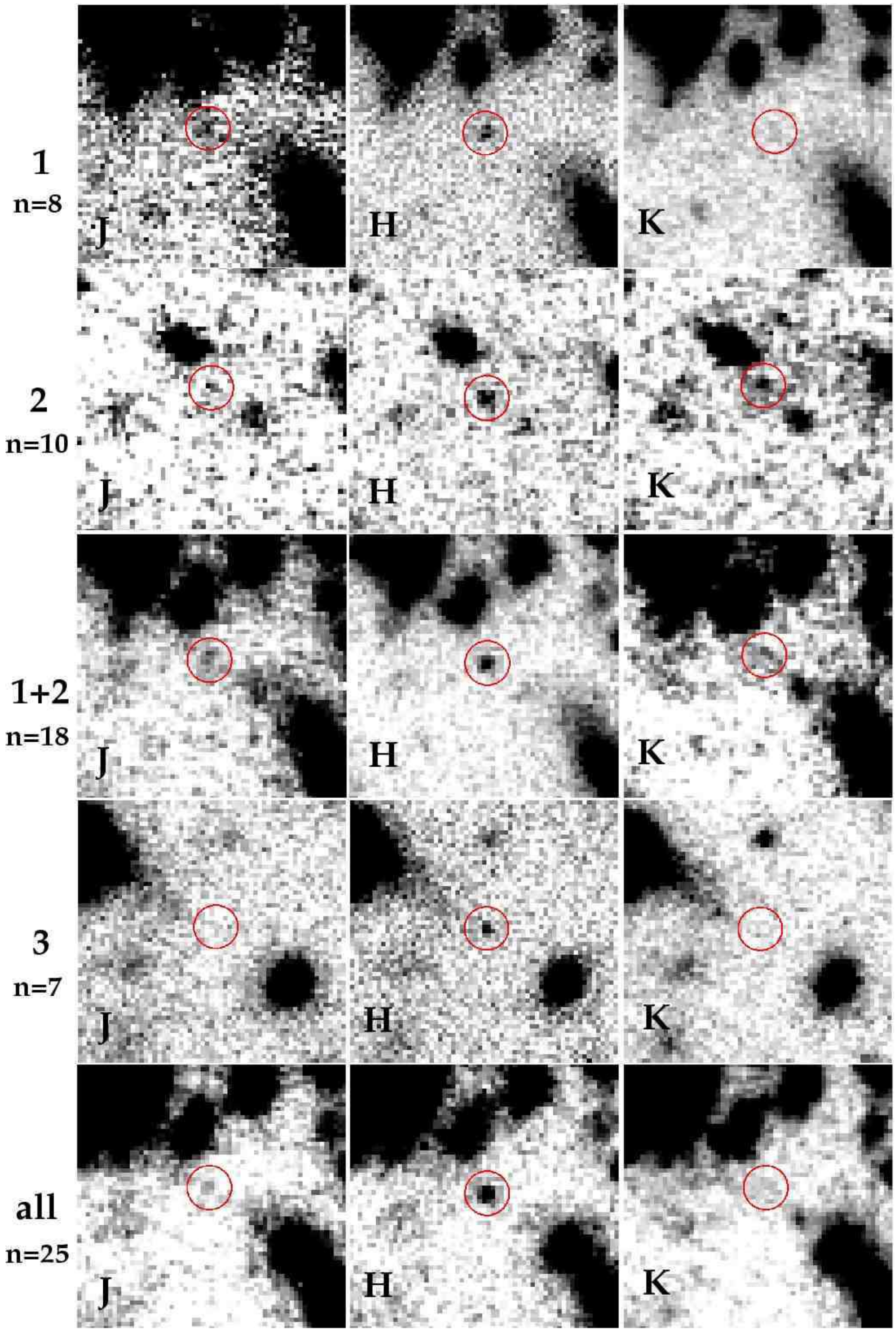

Fig. B.1. From left to right, stacked J, H and Ks images for first, second, third, first + second-category and all $z \geq 6$ candidate sources in Abell 1835 and AC114, excluding EROs. Images display a $10'' \times 10''$region around the composite source.

SExtractor detection parameters to these images, and compared the detection results. This procedure has some obvious limitations, because the final stacks are not independent from the original H-band detection images. For Abell 1835, $\sim$ 89% of the first and second-category sources presented in Table C.2 are re-detected in the pseudo-χ^2 image, with positions less than 1 pixel off with respect to original centroids, except #13 and #15. For AC114, 75% of the first and second-category sources are re-detected in the pseudo-χ^2 image (all sources except #2 and #5). By definition, third-category sources are clearly detected only in the H band image. However, sources #21 and #35 in Abell 1835 are also re-detected in the corresponding pseudo-χ^2 images. On the other hand, 60(86)% of the first and second-category high-z sources in Abell 1835 (AC114)

Table B.1. Expected percentage of false-positive detections in our samples of third-category (only detected in H-band) and second/first-category (detected in H- and at least another near-IR band) dropouts for each cluster, as a function of the detection filters and the H-band magnitude. The typical errors in these values are ~ 15 and ~ 30 for Abell 1835 and AC114, respectively.

	3rd Cat.	First / Second Category dropouts						
H range	H	SZ+H	J+H	H+K	SZ+J+H	J+H+K	SZ+H+K	SZ+J+H+K
[mags]	% of spurious detections in Abell 1835 (AC114)							
22.75 - 23.00	0 (0)	0	0 (0)	0 (0)	0	0 (0)	0	0
23.00 - 23.30	35 (57)	27	12 (25)	25 (33)	12	12 (33)	12	12
23.30 - 23.75	98 (100)	66	65 (88)	61 (61)	28	27 (38)	30	12
23.75 - 24.00	100 (100)	56	96 (100)	73 (100)	27	28 (100)	40	11

(Tables C.2 and C.3) are re-detected in at least another near-IR filter with a mean S/N≥ 2 within a 1.5″-diameter aperture. Thus, a majority of our optical dropouts, at least the first and second-category ones, have a significant signal detected in several near-IR bands.

C.2. Transient objects

We have estimated the contamination level expected in our images due to known transients, such as TNOs or supernovae, taking into account the combination schemes used to build the final stack, which typically reject $10-20\%$ of the brightest pixels at this stage. The typical motions observed and expected for TNOs range between $\sim (1-10)''/h$ (Trujillo et al. 2001). In the detection H band a TNO moves at least between 3 and 6 pixels in 10% of the exposure time, depending on overhead details and the distribution of exposures during the observing period, thus making a TNO selection highly unlikely. On the contrary, supernovae events within the cluster, and particularly a type I supernova in the halo of a cluster member, cannot be removed with the usual scheme. We do not expect more than 1-2 events per cluster in these deep observations, according to previous findings (e.g., Gal-Yam et al. 2002). Very rare and unique events, such as lensed supernovae (e.g. Marri & Ferrara 1998, Marri et al. 2000), or a tidal disruption of a star by a BH (cf. Stern et al. 2004) cannot be excluded either, but again such events are not expected to dominate the sample.

C.3. Photometric stability

The Abell 1835 data in the SZ band were obtained at two different epochs: 19 April 2004 ($\sim 4h$ exposure, 77 images) and 15 May 2004 ($\sim 2h$ exposure, 45 images). Both series of images have identical seeing and photometric zeropoints. We used these data to check the compatibility of our magnitude measurements at different epochs, and particularly to set constraints on the possible variability of faint optical dropouts in these bands. Among the 9 sources detected in the SZ band, 7 of them show magnitudes and 1σ error-bars (with $\sigma_{SZ} \sim 0.1$ to 0.5 mag) fully consistent between the two epochs and with the final stack. A bright and clearly variable source (A1835#4) and a particular case (A1835#8), both discussed in Sect. 7.4, are clear exceptions.

C.4. Stacked images

We have generated stacked J, H and Ks images for all first to third priority candidates, excluding EROs. A $10'' \times 10''$ region has been selected around the H-band centroid for each $z \geq 6$ candidate in Tables C.2 and C.3, for all $JHKs$ images. Multiplicative corrections have been applied to properly combine images coming from the two clusters with different photometric zero-points. After background subtraction, images have been averaged using IRAF routines and different pixel rejection schemes in order to obtain a "clean" region around the stacked source, although the final photometry does not strongly depend on the combination procedure. Representative results are displayed in Fig. B.1, for first to third-category sources combined in different ways. We used Sextractor to measure the corresponding fluxes, best magnitudes and errors of these composite sources in the different bands and samples. Colors are obtained using the same apertures as for individual sources. Results are summarized in Table C.1. The S/N of the composite sources in all filters increases with the number of stacked images, as expected if a significant signal was present in a majority of sub-images and bands. Although these optical dropouts are likely to constitute a non-homogeneous sample, all the stacked series display a break between J and H (typically $J-H \sim 1.5$ to 2.50 in the Vega system), and relatively blue $H-Ks$ colors, thus a photometric SED corresponding to a dominant population of $z \geq 8$ sources (see Fig. 2), or a noticeable contamination by spurious sources. The flux detected in the J band is clearly higher for the first and first + second-category dropouts, i.e. the brightest sources in the H band, as expected if a fraction of these sources are at $z \leq 8$. This result is the same when combining all dropouts at $z \leq 8$ (6 sources, all of them first or second-category), but the final S/N in this band is higher when blindly combining all first + second-category dropouts. The same comments stand for the Ks band, for which the best S/N is achieved for the first and second-category dropouts. The profiles obtained for the composite sources in the different filters are all compatible with the seeing values in the H band ($\sim 0.5''$), and slightly broader in J and Ks ($\sim 0.55''$and $0.45''$respectively).

False or transient sources stacked in these images will tend to enhance the trend towards artificially "blue" $H-Ks$ and "red" $J-H$ colors, thus providing an independent method to estimate the contamination levels reported in Table B.1, and applied throughout the paper. For $z \geq 6$ candidates stacked here, $H-K$ colors provide a rough estimate of the restframe UV slope β. For young starbursts, β is found to be ~ -2.5 in the local universe (Heckman et al. 1998), $\beta \sim -3$ for the $z \sim 7-8$ candidates reported by Bouwens et al. (2004b), and it could reach values up to $\beta \sim -3$ for young starbursts at very low metallicity (see Fig. 1 from Schaerer & Pelló 2005). As discussed in Sect. 8.1, our high-z candidates tend to be extremely blue in $H-K$, but none of them could be excluded from the sample to a 3σ level on the basis of a clear $\beta \leq -3.5$, although two first category dropouts are close to this limit (A1835#7 and AC114#2, see also Sect. 8.1). Note that the contamination here refers to the *integrated light* in the H band, whereas Table B.1 reports percentages in the number of sources. The results are the following:

- The extremely blue colors of the third-category sample argue for a significant contamination, between 60 and 65% of the total light for β ranging between -3.5 and -2.5 respectively. The faint population of third category dropouts could be dominated by spurious sources, as already expected from Table B.1.
- The second-category sample is compatible with a very low contamination level by spurious sources. It is negligible for $\beta \sim -3.5$, and it could reach up to 10% for $\beta \sim -2.5$.
- The combined first-category image is clearly dominated by the brightest sources, and among them the two dropouts reach close to $\beta \leq -3.5$ at 2-3σ level (Sect. 8.1). This gives a contamination level ranging between 62 and 70% for the whole sample, whereas it is ∼10% when these two sources are removed. Note that these sources are detected in several bands.
- The combined first + second category (with all sources included) is qualitatively in good agreement with expectations in Table B.1 (i.e. 33 to 50% maximum contamination on the whole sample).

Overall, the contamination levels based on UV slope considerations are optimistic in general as compared to the blind corrections applied according to Table B.1.

C.5. Spatial distribution of optical dropouts

We carried out a Kolmogorov-Smirnov (hereafter K-S) monodimensionnal test (Peacock, 1983) on the observed radial distance of the sources with respect to the cluster central galaxy, because high redshift images are expected to be preferentially found around the critical lines for positive magnification bias (Broadhurst et al. 1995), and thus inconsistent with a homogeneous distribution. Such positive bias is expected to be the case when probing the steep part of the luminosity function (see Sect. 8.2 and Fig. 12). When comparing our candidates with a uniform distribution (after masking the usual regions of the image), we obtain an average to high resulting probability ($\sim 40\%$ for Abell 1835, $\sim 2\%$ for AC114). Thus, the K-S test indicates that the spatial distribution of our candidates has a low probability to be drawn from a homogeneous distribution. However, applying a similar K-S test for the spurious sources used in Sect. 5.3 gives us much lower probabilities ($< 0.01\%$) for the false-positive detections to be drawn from a homogeneous distribution. Such a high clustering level is expected for spurious detections, usually concentrated in specific regions of the image having a high noise level. When comparing the distribution of candidates and false-positive detections in the same K-S test, we find that these two samples are likely to have a different distribution (with probability $< 0.01\%$ to be drawn from the same parent distribution).

Table C.1. Photometric magnitudes and colors derived for the composite $z \geq 6$ source candidates in Abell 1835 and AC114 (see text for details). Upper limits correspond to 3 σ.

Combination	J	H	Ks	$J-H$	$H-Ks$
1st category dropouts	25.28 ± 0.20	23.68 ± 0.09	≥ 24.7	1.71	≤ -1.0
2nd category dropouts	25.69 ± 0.23	24.02 ± 0.08	23.80 ± 0.13	2.20	0.48
3rd category dropouts	≥ 25.6	23.79 ± 0.10	≥ 24.7	≥ 1.82	≤ -0.92
1st + 2nd category dropouts	25.38 ± 0.17	23.81 ± 0.08	24.22 ± 0.15	1.53	-0.32
1st + 2nd + 3rd category dropouts	26.18 ± 0.31	23.84 ± 0.07	24.76 ± 0.24	2.45	-0.86

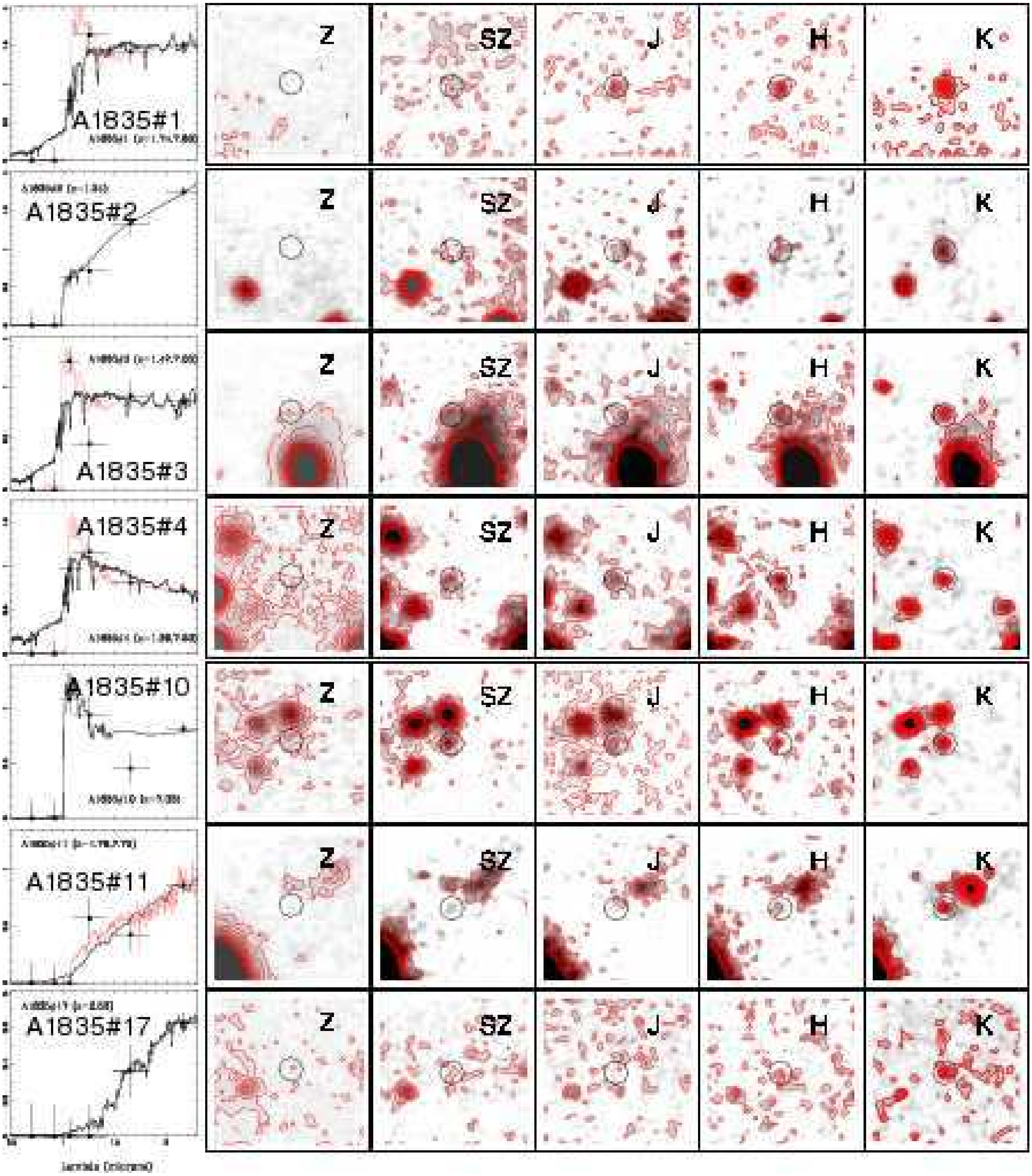

Fig. C.1. (2 pages) Close-up of the best candidates in Abell 1835, showing the object and their surrounding 10 × 10 arcsecs field. Objects satisfying the ERO criterion ($R - Ks > 5.6$) are presented above, and other first or well-detected second-category candidates are given in the next page. The FORS-Z band (non-detection criterion), and the ISAAC-NIR bands are displayed in linear scale, from -3σ to 6σ levels. Contours are for background level + 1, 2, 3, ... σ respectively. On the left is the SED in the $RzSZJHK$ bands and the best photometric redshift solutions obtained. When two possible solutions coexist, the higher redshift fit is displayed with a red dotted line. Fluxes values are given in f_λ, with units multiple of 10^{-19} ergs s^{-1} cm^{-2}.

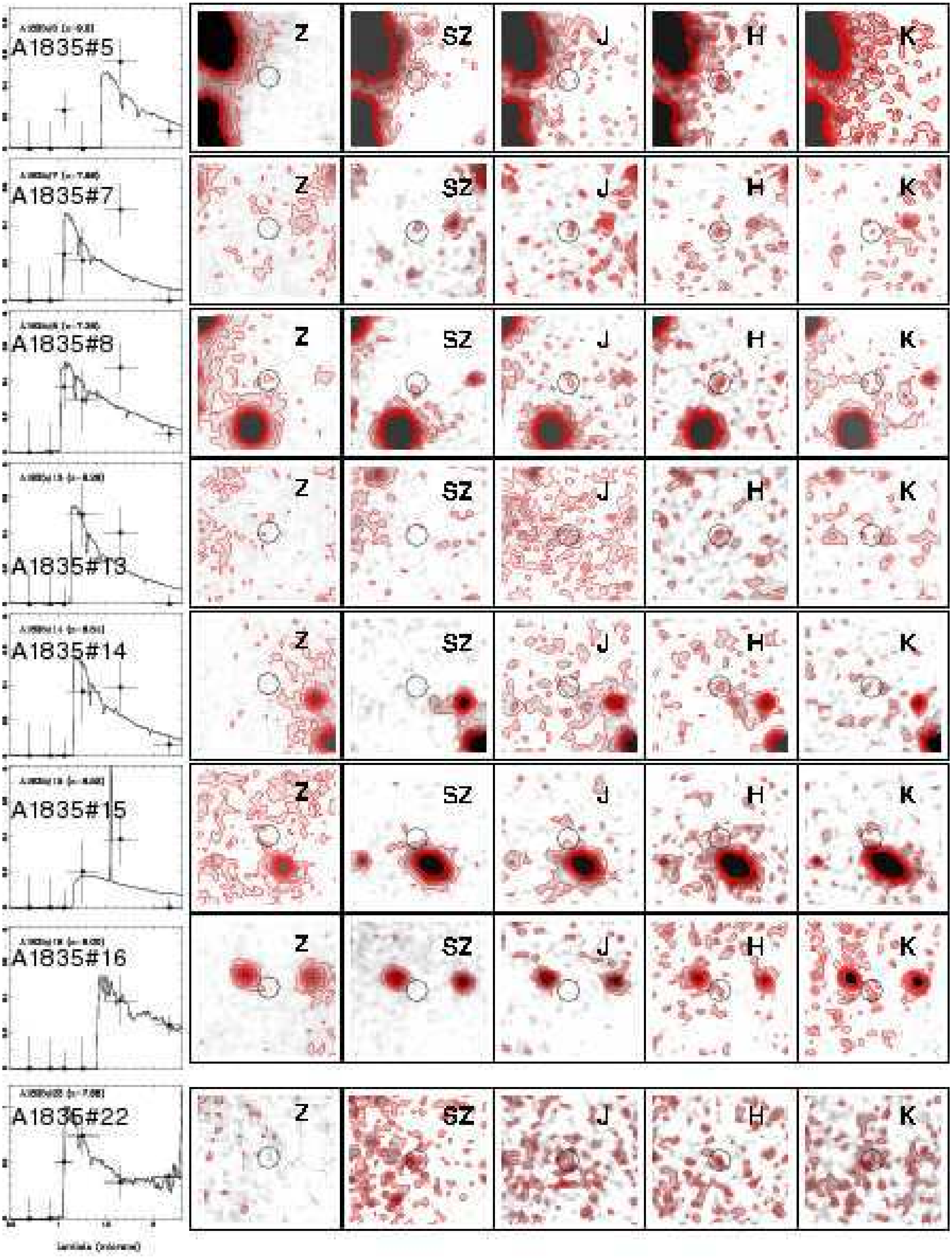
A1835#5
Z
SZ
J
H
K
A1835#7
A1835#8
A1835#13
A1835#14
A1835#15
A1835#16
A1835#22
lambda (microns)

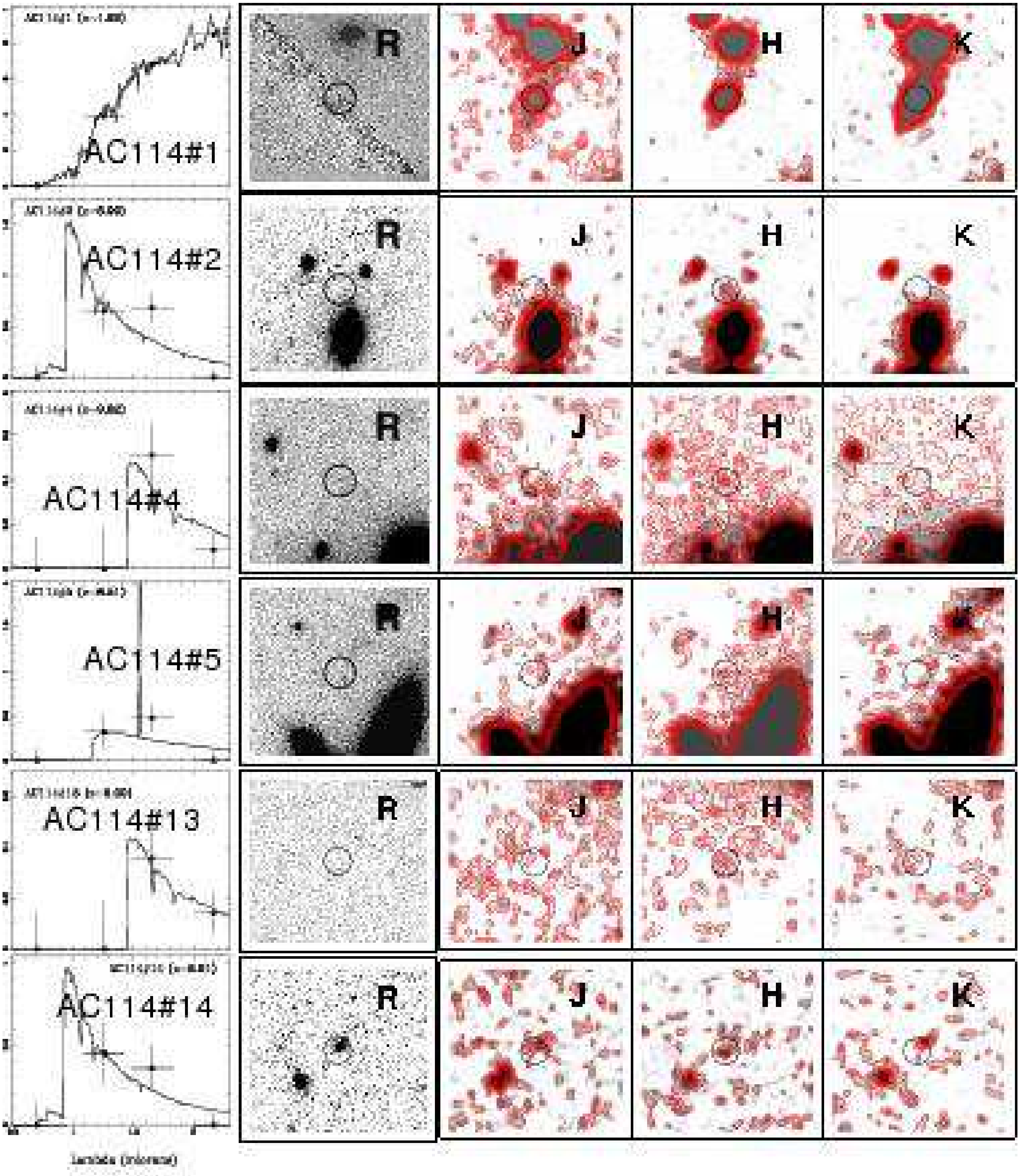

Fig. C.2. Same figure as C.1, for best-detected first and second-category candidates in AC114. Close-ups correspond to the HST-R and ISAAC-NIR bands.

ID	RA (14:)	DEC (02:)	SZ	J	H	K	$\phi\ z$	z range	$\tilde{z}$	μ_6	μ_{10}	$\tilde{\mu}$	L_{1500} $10^{40} erg\ s^{-1}$ Å^{-1}	SFR $M_\odot\ yr^{-1}$	notes
First-category dropouts															
#1	0:58.278	50:26.65	24.56 ± 0.18	23.14 ± 0.11	22.22 ± 0.10	21.10 ± 0.04	A	[6.3-8.1]	7.80	1.27	1.27	1.28	79.5	83.5	Ex. ERO
								[1.3-1.9]	1.74	-	-	-	-	-	
#2	0:57.538	52:49.85	24.80 ± 0.22	24.05 ± 0.27	22.29 ± 0.11	20.95 ± 0.03	A	[1.18-1.64]	1.34	-	-	-	-	-	Ex. ERO (1)
#3	1:01.484	51:03.63	24.03 ± 0.11	24.54 ± 0.42	22.69 ± 0.16	21.71 ± 0.07	A	[6.7-7.3]	7.05	1.64	1.66	1.65	12.7	13.3	Ex. ERO
								[1.1-1.7]	1.47	-	-	-	-	-	
#4	1:01.733	51:05.26	24.31 ± 0.14	23.50 ± 0.16	22.82 ± 0.18	21.90 ± 0.08	A	[6.2-7.8]	7.53	1.67	1.7	1.69	39.6	41.6	Ex. ERO
								[1.2-1.8]	1.57	-	-	-	-	-	
#5	1:07.034	51:35.71	25.82 ± 0.52	> 25.60	23.24 ± 0.28	23.91 ± 0.55	B	[8.0-10.0]	(9.00)	1.92	1.96	1.96	28.6	30.1	
#7	1:05.067	50:57.52	25.81 ± 0.51	25.34 ± 0.89	23.39 ± 0.32	> 24.70	B	[6.4-8.0]	7.66	1.53	1.55	1.54	10.1	10.6	
#8	1:00.058	52:44.08	25.36 ± 0.34	24.99 ± 0.64	23.40 ± 0.32	24.00 ± 0.60	B	[6.1-8.0]	7.38	110.81	86.53	> 25	< 0.6	< 0.7	Ex. (2)
#10	0:59.890	50:57.59	24.18 ± 0.12	23.74 ± 0.20	23.45 ± 0.33	21.77 ± 0.07	A	[6.8-7.7]	7.33	1.49	1.51	1.50	33.1	34.8	Ex. ERO
								[1.1-1.7]	1.47	-	-	-	-	-	
#11	1:06.182	50:27.74	> 26.90	24.29 ± 0.33	23.54 ± 0.36	21.72 ± 0.07	C	[7.0-8.5]	(7.75)	1.31	1.32	1.32	25.4	26.7	Ex. ERO
								[0.8-2.5]	1.78	-	-	-	-	-	
#13	1:03.125	51:28.81	> 26.90	24.41 ± 0.38	23.58 ± 0.38	> 24.70	A	[8.0-9.2]	8.29	2.2	2.26	2.24	14.9	15.6	
#14	1:04.209	51:54.55	> 26.90	24.77 ± 0.52	23.63 ± 0.39	24.53 ± 0.97	B	[7.3-10.0]	8.54	3.35	3.5	3.45	9.7	10.2	
#15	1:02.540	51:12.84	> 26.90	25.40 ± 0.94	23.63 ± 0.40	> 24.70	B	[7.5-10.5]	8.52	1.81	1.84	1.84	17.9	18.8	
#16	1:03.657	52:54.83	> 26.90	> 25.60	23.64 ± 0.40	23.08 ± 0.25	C	[8.0-10.0]	(9.00)	119.99	55.04	> 25	< 1.6	< 1.6	
#17	1:05.013	50:27.11	> 26.90	> 25.60	23.71 ± 0.43	22.06 ± 0.10	C	[1.48-5.05]	2.53	-	-	-	-	-	Ex. ERO
#22	1:02.551	51:30.06	25.00 ± 0.24	23.99 ± 0.25	23.81 ± 0.47	22.59 ± 0.16	A	[5.5-8.1]	7.68	2.28	2.34	2.31	17.8	18.7	
#23	1:05.699	51:52.92	> 26.90	24.93 ± 0.61	23.85 ± 0.48	24.03 ± 0.61	C	[8.0-10.0]	(9.00)	2.61	2.69	2.67	12.0	12.7	
#24	0:58.036	51:29.09	> 26.90	25.16 ± 0.75	23.88 ± 0.50	> 24.70	C	[8.0-10.0]	(9.00)	1.6	1.62	1.62	19.3	20.2	
#27	1:04.299	51:57.19	> 26.90	> 25.60	23.93 ± 0.53	24.57 ± 1.01	C	[8.0-10.0]	(9.00)	3.54	3.71	3.68	8.1	8.5	
Second-category dropouts															
#6	0:59.659	50:54.73	> 26.90	> 25.60	23.37 ± 0.31	> 24.70	B	[8.0-10.0]	(9.00)	1.46	1.47	1.47	33.8	35.5	
#18	0:58.890	51:02.47	> 26.90	> 25.60	23.72 ± 0.43	> 24.70	C	[8.0-10.0]	(9.00)	1.47	1.48	1.49	24.4	25.6	
#19	1:00.138	52:05.20	> 26.90	> 25.60	23.72 ± 0.43	> 24.70	C	[8.0-10.0]	(9.00)	5.48	6.03	5.92	6.1	6.4	
#20	0:58.860	51:23.85	> 26.90	> 25.60	23.72 ± 0.43	> 24.70	C	[8.0-10.0]	(9.00)	1.67	1.69	1.69	21.3	22.4	
#21	0:58.732	51:53.86	> 26.90	> 25.60	23.76 ± 0.44	> 24.70	C	[8.0-10.0]	(9.00)	2.13	2.18	2.17	16.1	16.9	
#35	1:00.693	52:09.58	> 26.90	> 25.60	24.00 ± 0.56	24.25 ± 0.75	C	—	**1.68**	-	-	-	-	-	(3)

Table C.2. Photometric properties of Abell 1835 optical-dropouts. From left to right : identification number, astrometric position, near-IR photometry, photometric redshift quality (see Sect. 7.2 for details), redshift range $[z1 - z2]$ and applied redshift $\tilde{z}$, magnifications at $z = 6$ (μ_6), at $z = 10$ (μ_{10}), applied magnification ($\tilde{\mu}$), unlensed luminosity at rest-frame $\lambda = 1500$ Å .

Objects noted “ERO” satisfy the $(R - K > 5.6)$ criterion for Extremely Red Objects. For EROs with a best-fit solution at high-z, the low-z solution is also provided. “Ex” is mentioned in the notes for objects excluded from the discussion, and underlined photometric entries correspond to forced undetections in a given near-IR band after visual inspection (see text for details). All undetections are displayed with photometric upper limits, using the 1 σ limiting magnitudes inside a 1.5 $''$ diameter aperture given in table 1.
Bracketed values of $\tilde{z}$ are rough values based on the color-color selection diagrams.

[1] Near-IR counterpart of the sub-mm source SMMJ14009+0252 (Ivison et al. 2000, Smail et al. 2002).
[2] Also named A1835#1916 (Pelló et al. 2004a)
[3] Also named A1835#2582 (Richard et al. 2003)

N	RA (22:)	DEC (-34:)	J	H	K	ϕ z	z range	$\tilde{z}$	μ_6	μ_{10}	$\tilde{\mu}$	L_{1500} $10^{40} erg\ s^{-1}$ Å^{-1}	SFR $M_\odot\ yr^{-1}$	notes
First-category dropouts														
#1	58:49.777	46:54.95	22.19 ± 0.05	20.52 ± 0.02	19.23 ± 0.00	A	[1.58-1.89]	1.62	-	-	-	-	-	Ex., ERO
#2	58:49.040	47:21.94	24.14 ± 0.32	23.01 ± 0.22	$\underline{> 24.30}$	B	[6.3-9.2]	6.90	2.75	2.86	2.78	10.2	10.7	
#4	58:46.829	47:43.83	$\underline{> 25.50}$	23.33 ± 0.30	24.23 ± 0.99	B	[8.7-11.8]	9.82	13.68	10.98	11.20	6.1	6.4	
#5	58:46.505	47:25.96	24.90 ± 0.64	23.41 ± 0.32	> 24.30	B	[6.0-10.0]	8.51	10.1	12.62	12.10	3.3	3.5	
Second-category dropouts														
#13	58:44.972	49:17.27	> 25.50	23.72 ± 0.43	23.67 ± 0.59	C	[8.0-10.0]	(9.00)	1.54	1.57	1.57	23.1	24.2	
#14	58:53.511	48:37.85	24.55 ± 0.46	23.73 ± 0.44	> 24.30	A	[5.2-9.6]	6.91	2.73	2.84	2.76	7.1	7.4	
#16	58:50.243	48:35.75	24.55 ± 0.46	23.90 ± 0.51	$\underline{> 24.30}$	A	[5.2-9.6]	6.88	23.21	15.42	21.35	0.9	0.9	
#19	58:43.844	47:35.31	> 25.50	23.98 ± 0.55	23.69 ± 0.60	C	[8.0-10.0]	(9.00)	3.31	3.51	3.49	8.1	8.6	
Third-category dropouts														
#15	58:53.529	49:13.45	> 25.50	23.75 ± 0.45	> 24.30	C	[8.0-10.0]	(9.00)	4.88	5.31	5.24	6.7	7.1	
#17	58:47.551	48:53.51	> 25.50	23.93 ± 0.53	> 24.30	C	[8.0-10.0]	(9.00)	2.85	2.97	2.96	10.1	10.6	

Table C.3. Photometric properties of AC114 candidates. Caption is the same as in Table C.2.